Graal Apparatus

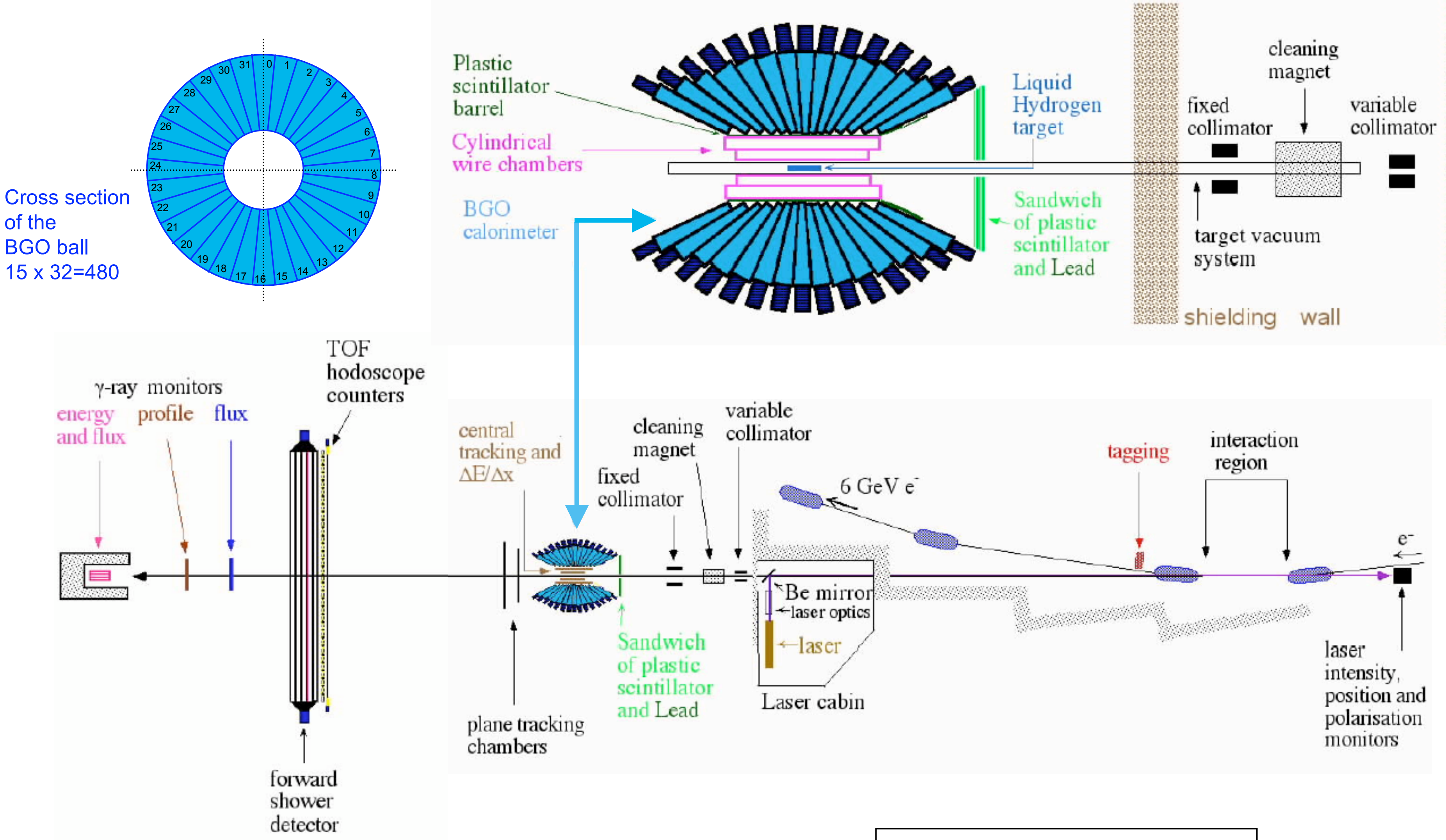

NOT IN SCALE

$\gamma + n + (p) \rightarrow \pi^{\circ} + n + (p)$ $\Delta\theta Vs \Delta\phi$

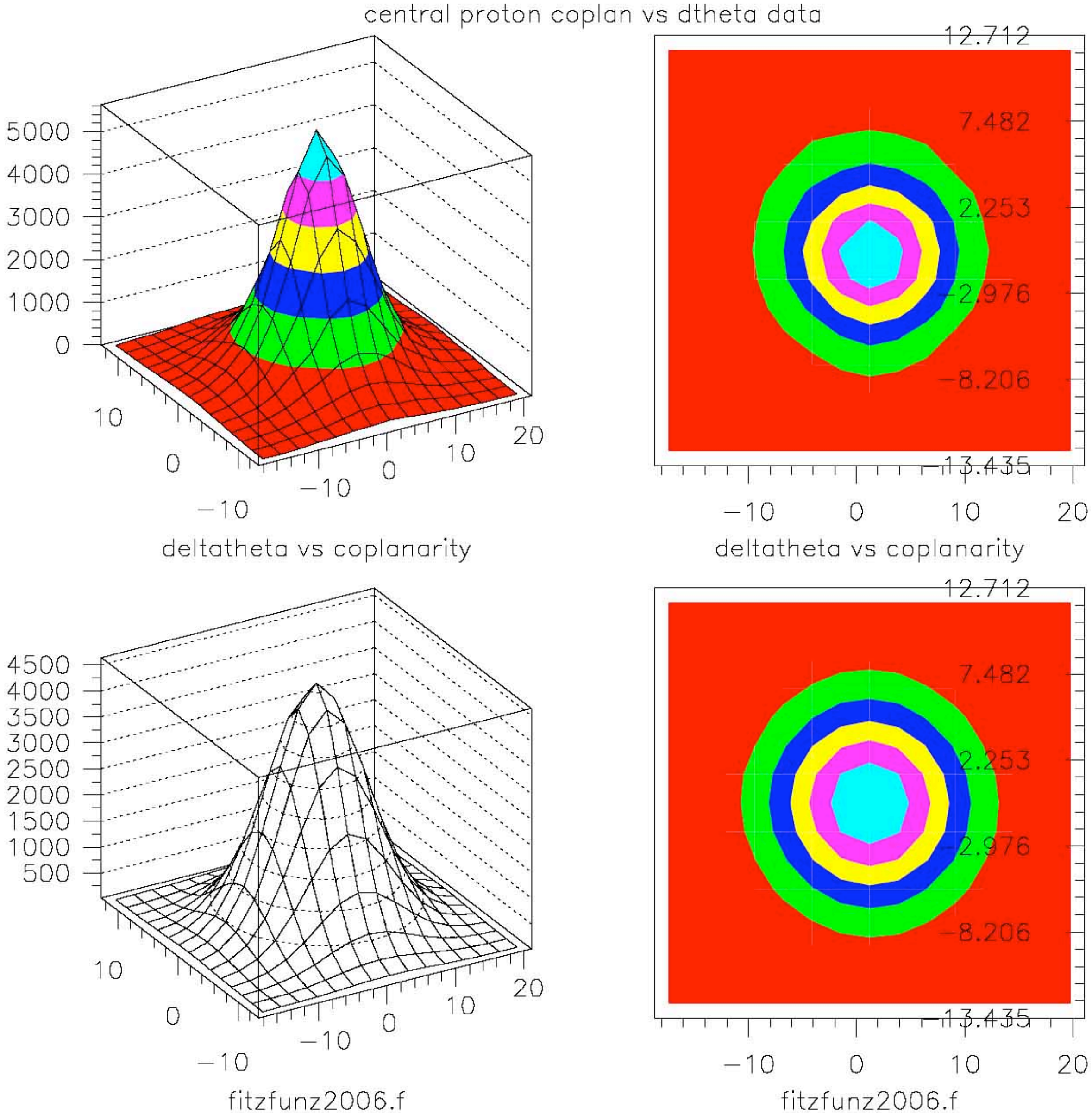

$\gamma + n + (p) \rightarrow \pi^{\circ} + n + (p)\ E_{cal}/E_{mis} VsMM\eta$

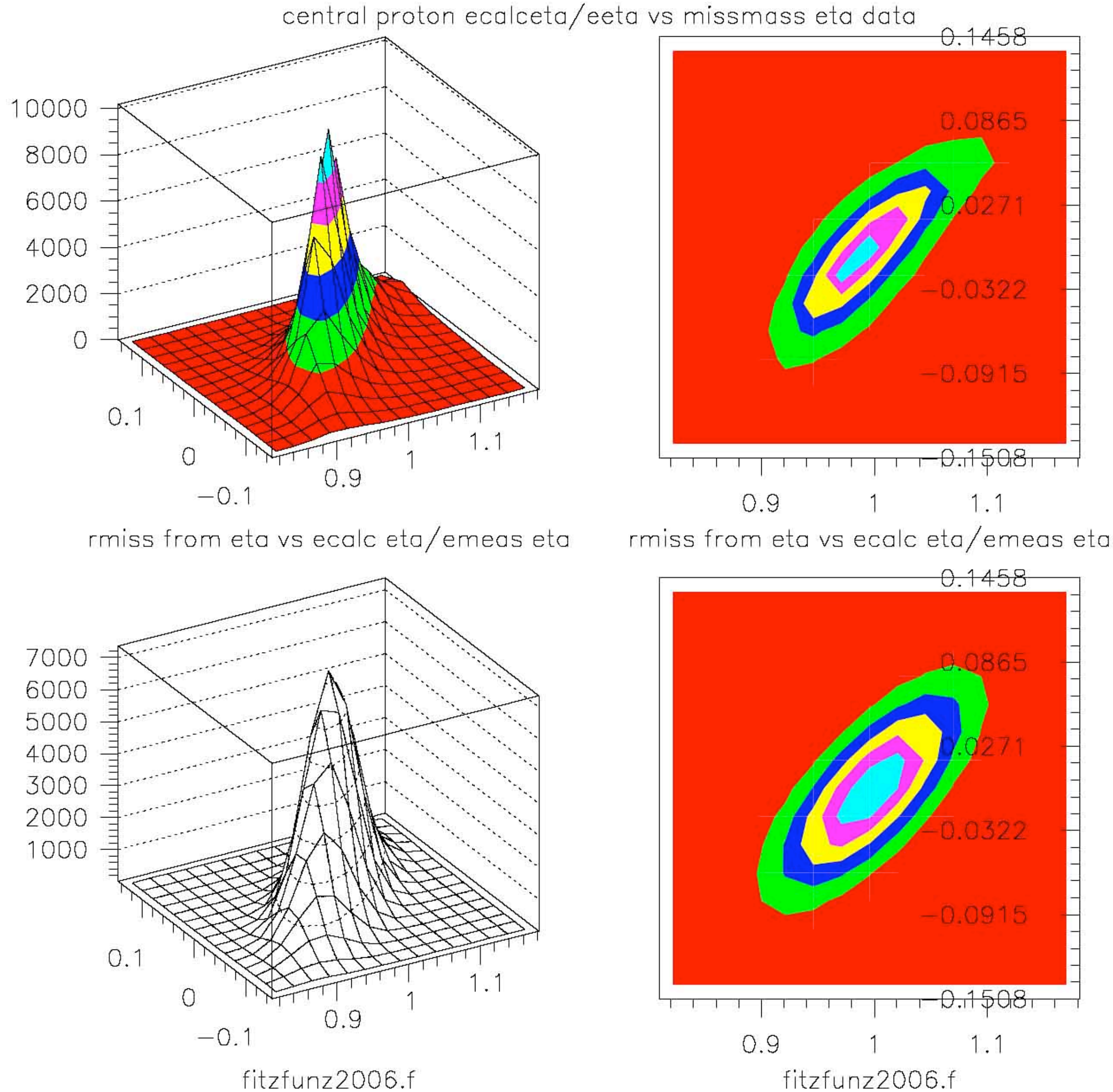

$\gamma + n + (p) \rightarrow \pi^\circ + n + (p)$ InvMass

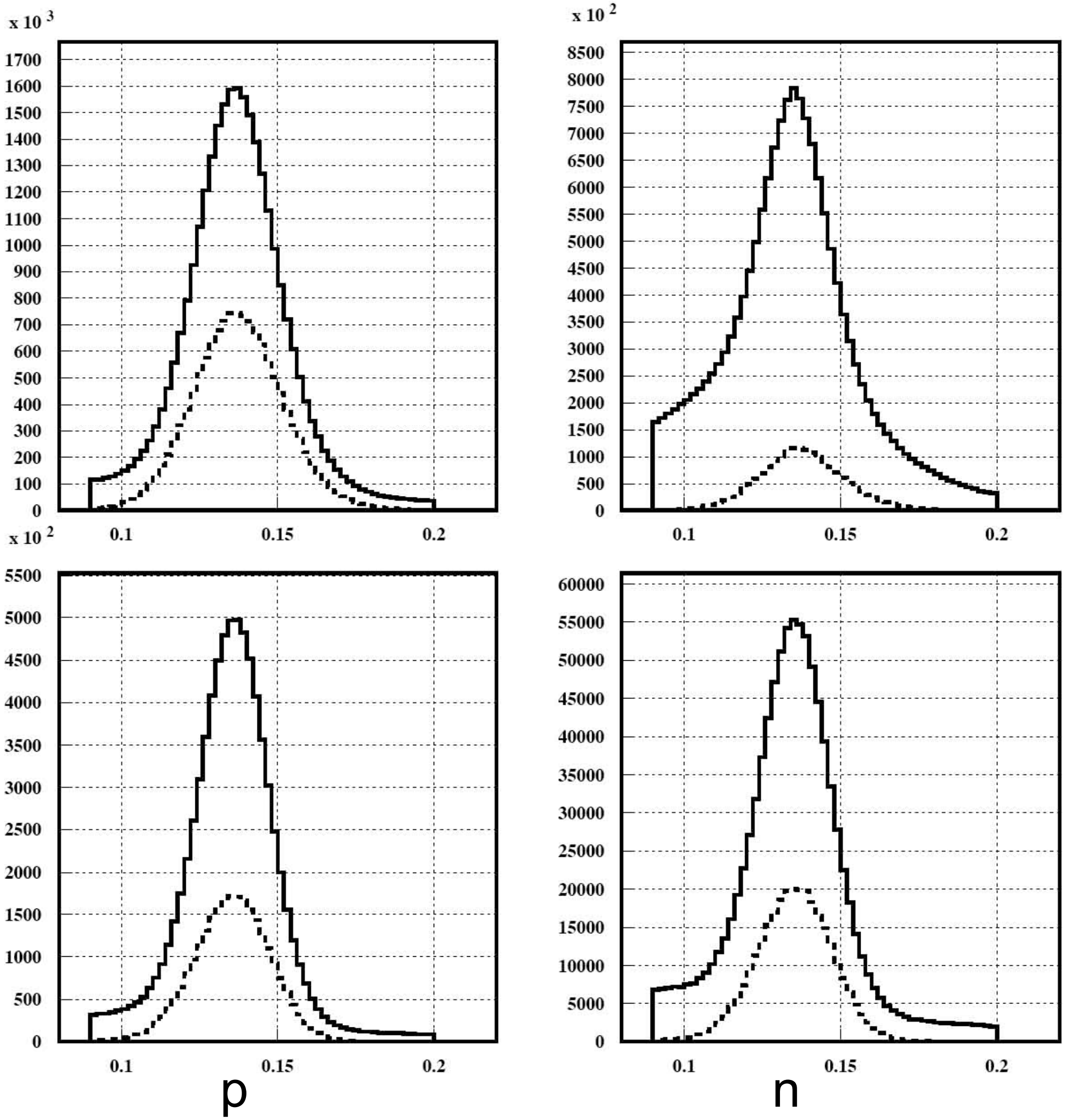

$\gamma + n + (p) \rightarrow \pi^\circ + n + (p)$ fp/qfp

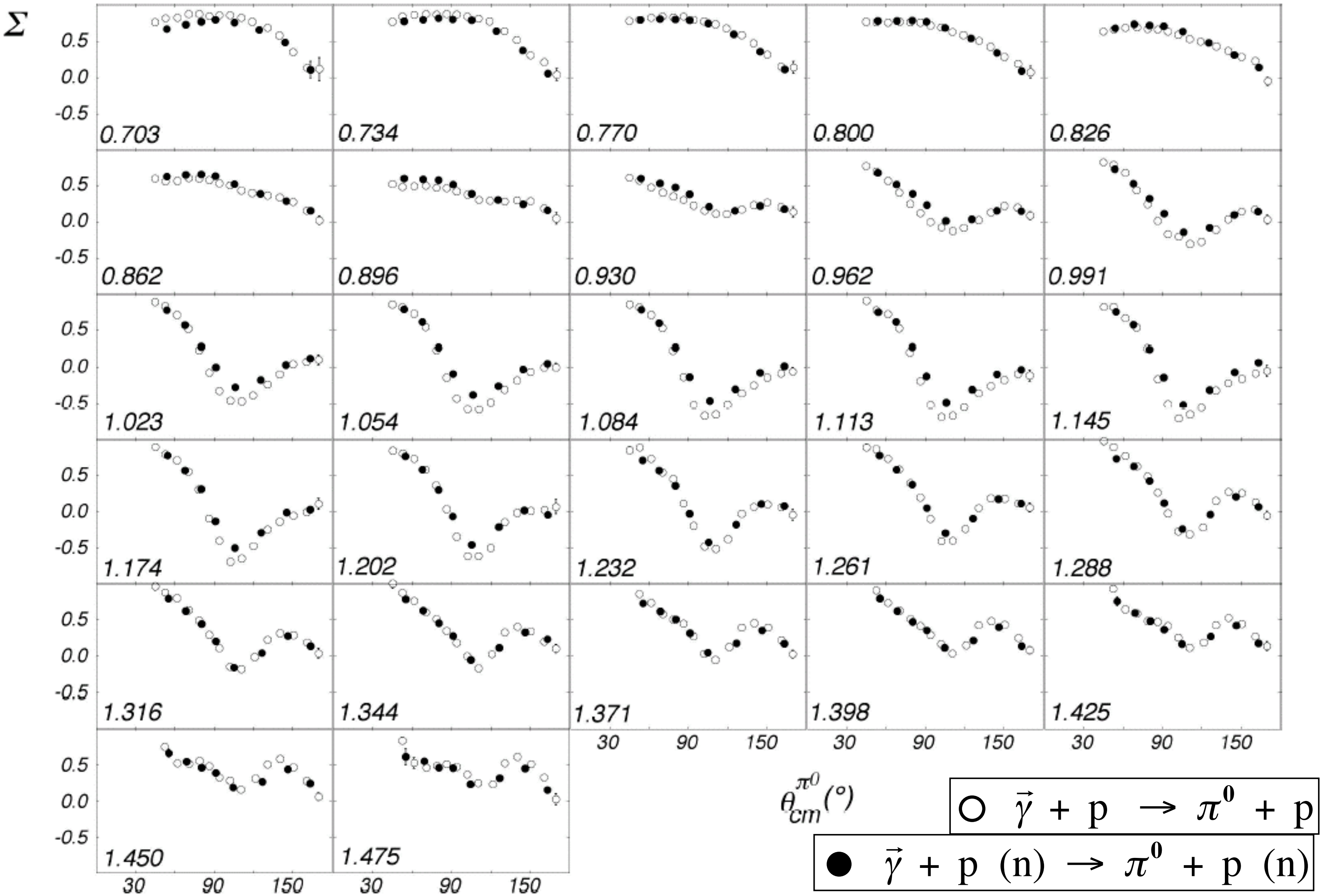

$\gamma + n + (p) \rightarrow \pi^\circ + n + (p)$ qfn/qfp   0.70-0.96 GeV

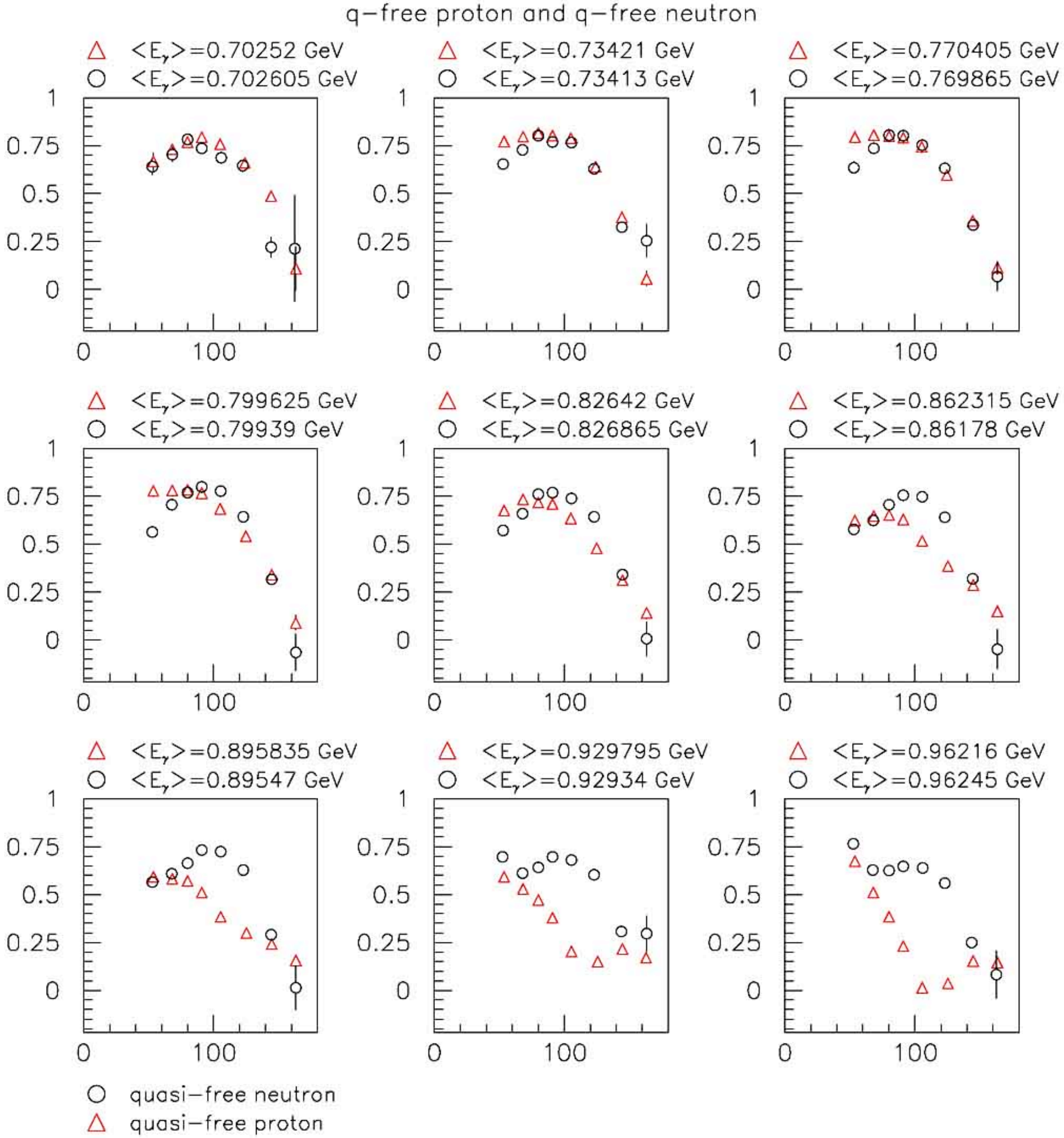

π° quasi-free proton vs quasi-free neutron 0.70-0.96 GeV

$\gamma + n + (p) \rightarrow \pi^\circ + n + (p)$ qfn/qfp 0.99-1.23 GeV

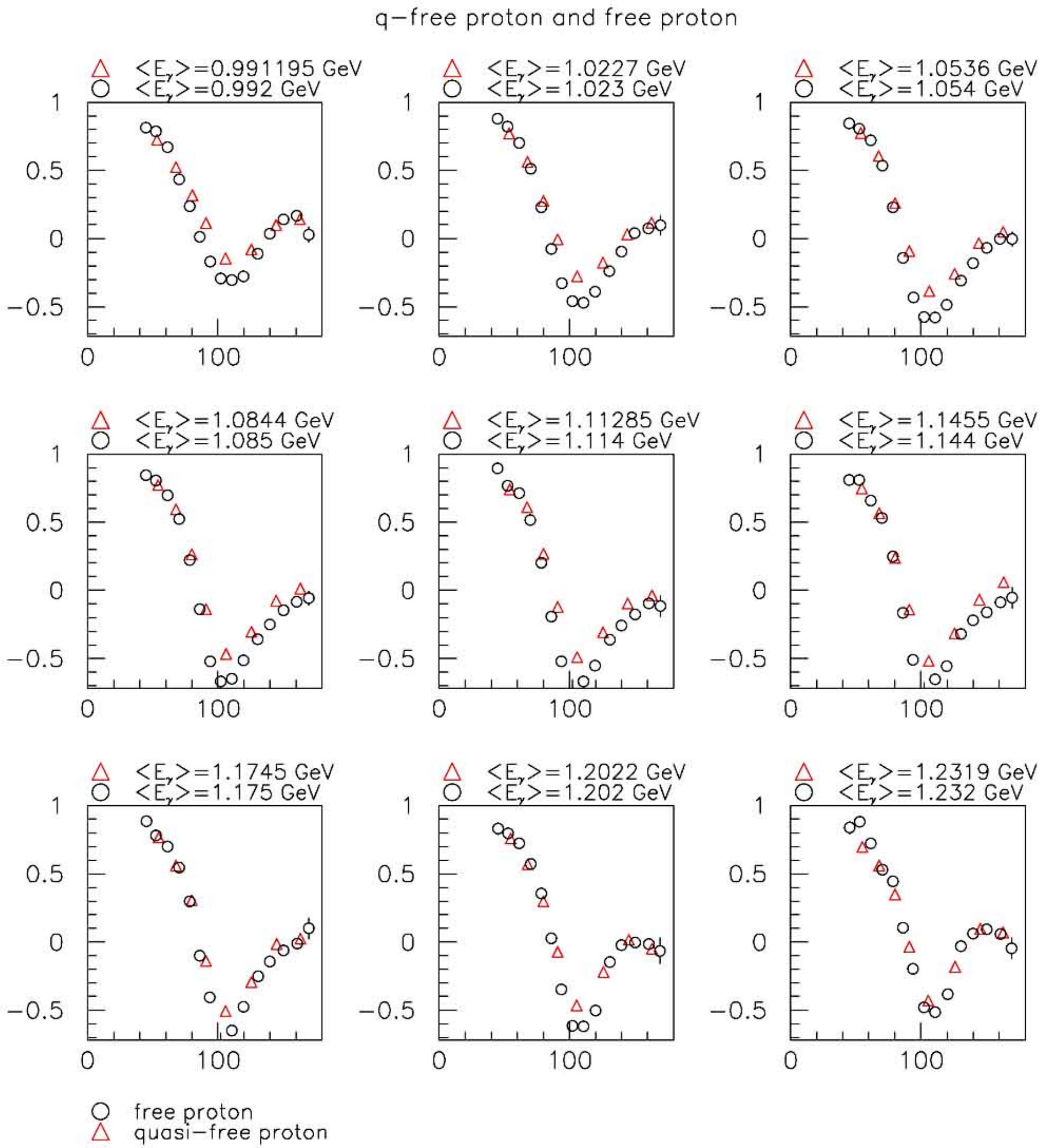

π° quasi-free proton vs quasi-free neutron 0.99-1.23 GeV

$\gamma + n + (p) \rightarrow \pi^\circ + n + (p)$ qfn/qfp 1.26-1.47 GeV

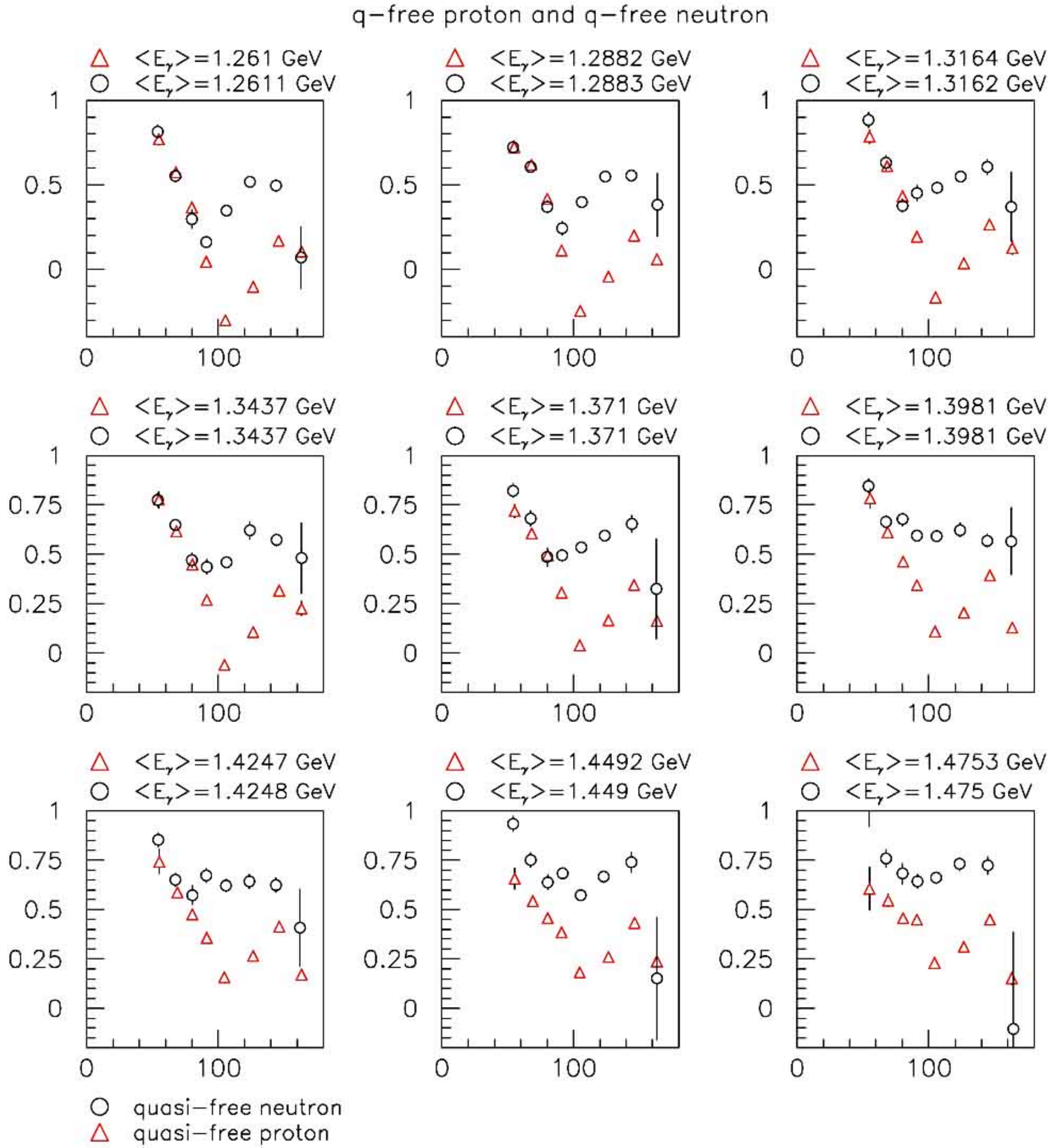

π° quasi-free proton vs quasi-free neutron 1.26-1.47 GeV

γ + n + (p) ➔ π° + n + (p)   qfn

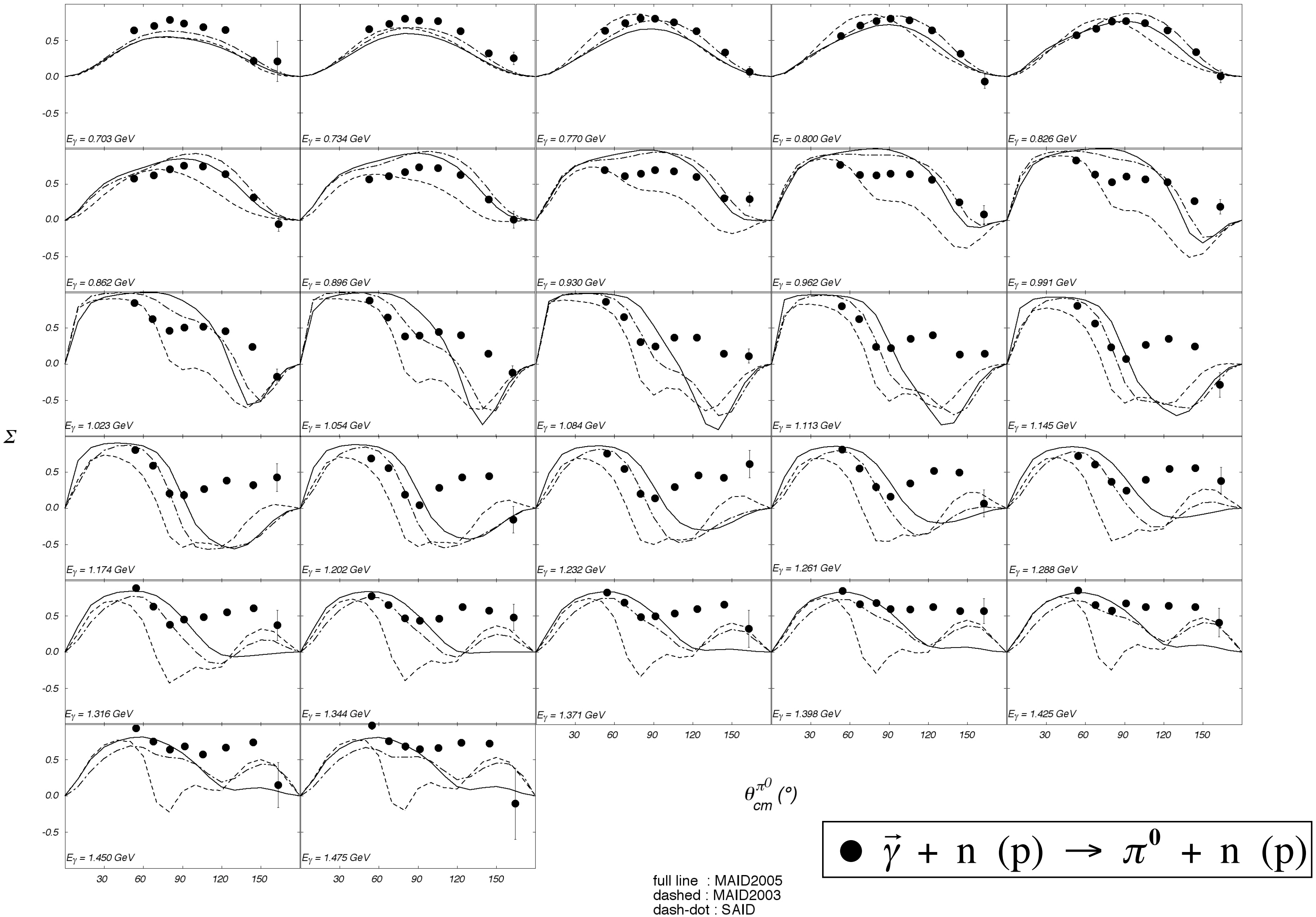

Σ
E_γ = 0.703 GeV
E_γ = 0.734 GeV
E_γ = 0.770 GeV
E_γ = 0.800 GeV
E_γ = 0.826 GeV
E_γ = 0.862 GeV
E_γ = 0.896 GeV
E_γ = 0.930 GeV
E_γ = 0.962 GeV
E_γ = 0.991 GeV
E_γ = 1.023 GeV
E_γ = 1.054 GeV
E_γ = 1.084 GeV
E_γ = 1.113 GeV
E_γ = 1.145 GeV
E_γ = 1.174 GeV
E_γ = 1.202 GeV
E_γ = 1.232 GeV
E_γ = 1.261 GeV
E_γ = 1.288 GeV
E_γ = 1.316 GeV
E_γ = 1.344 GeV
E_γ = 1.371 GeV
E_γ = 1.398 GeV
E_γ = 1.425 GeV
E_γ = 1.450 GeV
E_γ = 1.475 GeV
$\theta_{cm}^{\pi^0}$ (°)
● $\vec{\gamma}$ + n (p) → π^0 + n (p)
full line : MAID2005
dashed : MAID2003
dash-dot : SAID

$\gamma + n + (p) \rightarrow \eta + n + (p)$ $\Delta\theta/\Delta\phi$

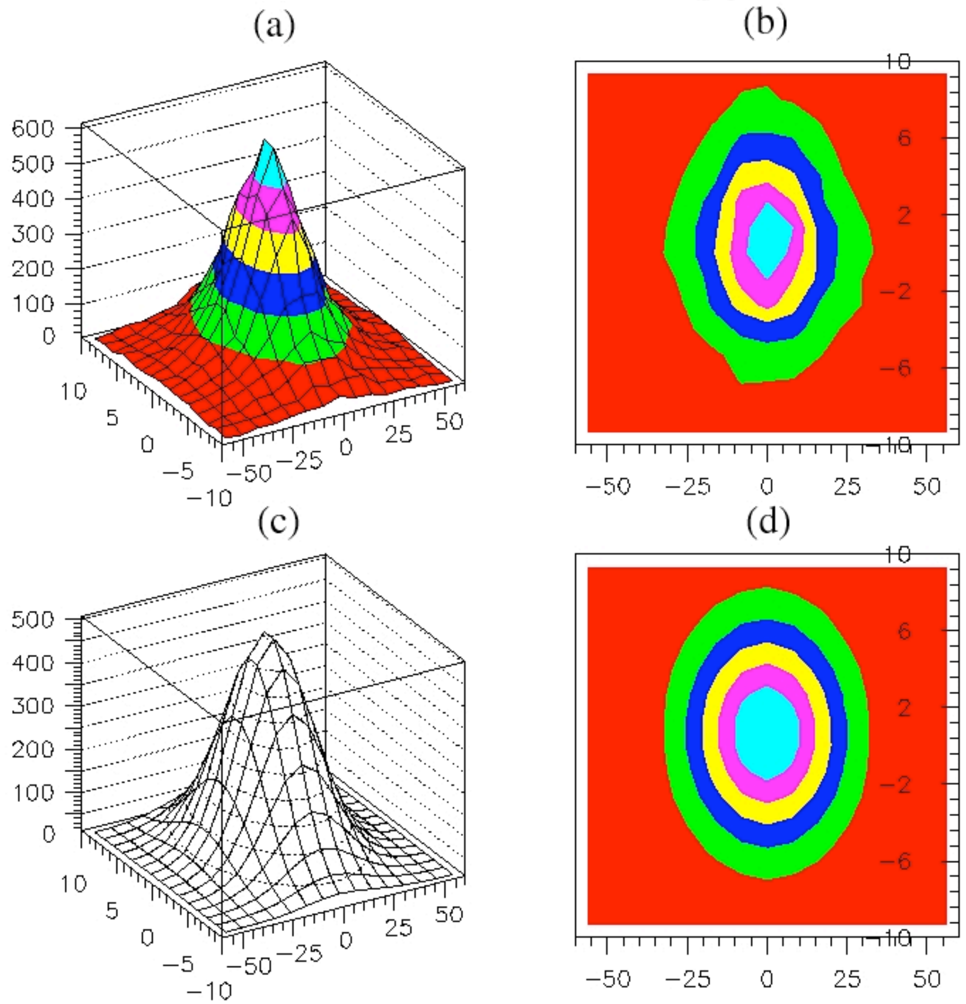

FIG. 1: Upper part: The correlation $\Delta\theta$ vs. ($\Delta\phi$-180°) in three-dimensional view(a) and its projection on two dimensions (b); Lower part: The bidimensional gaussian fit (c) and its projection on two dimensions (d).

$\gamma + n + (p) \rightarrow \eta + n + (p)$ $E^{\eta}_{cal}/E^{\eta}_{meas}$

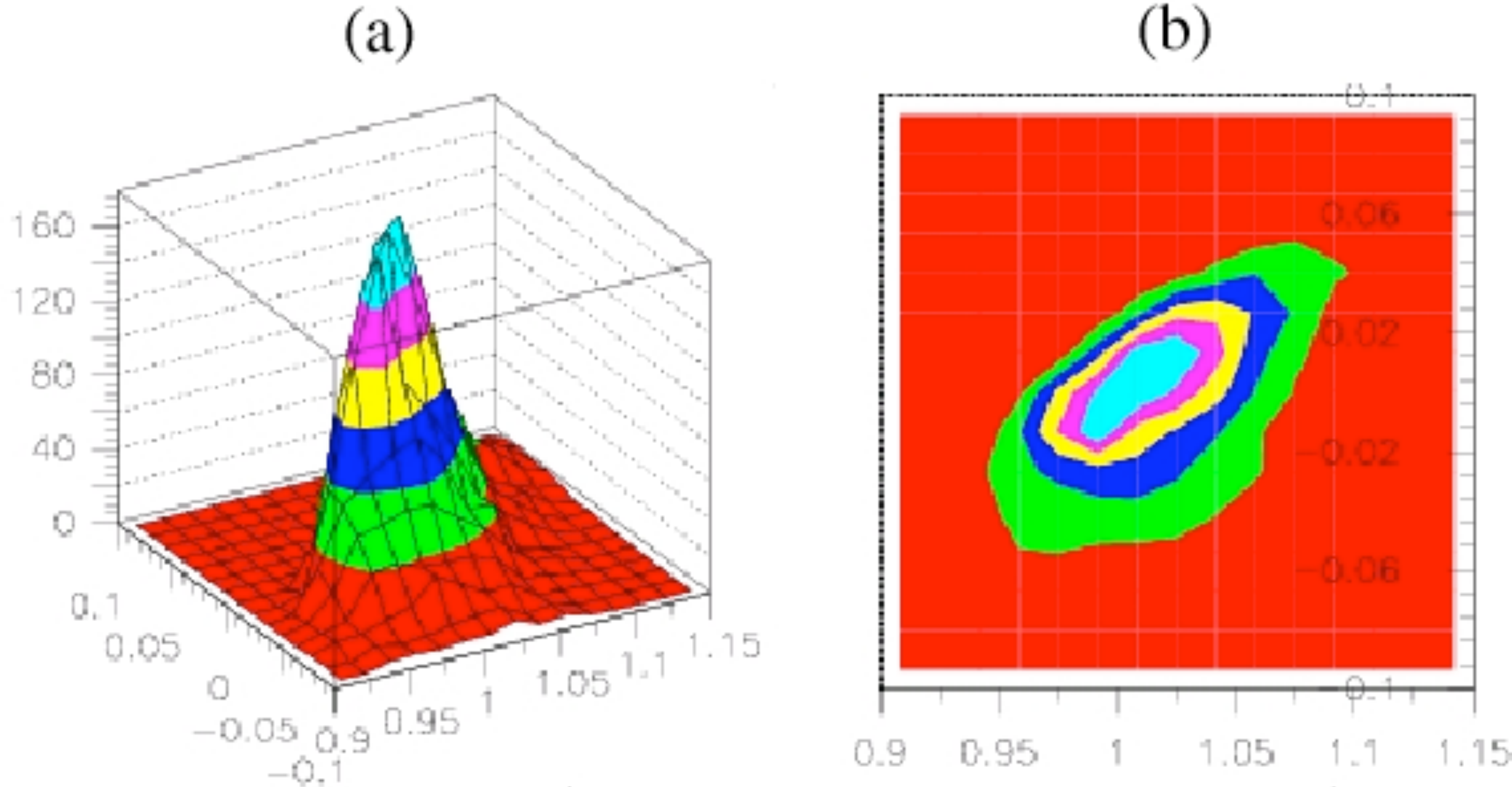

FIG. 2: The three-dimensional correlation $E_{\eta}^{calc}/E_{\eta}^{meas}$ vs. (M_X- M_N) (a) (see text for explanation) and its projection on two dimensions (b).

$\gamma + n + (p) \rightarrow \eta + n + (p)$ Copl + Fermi

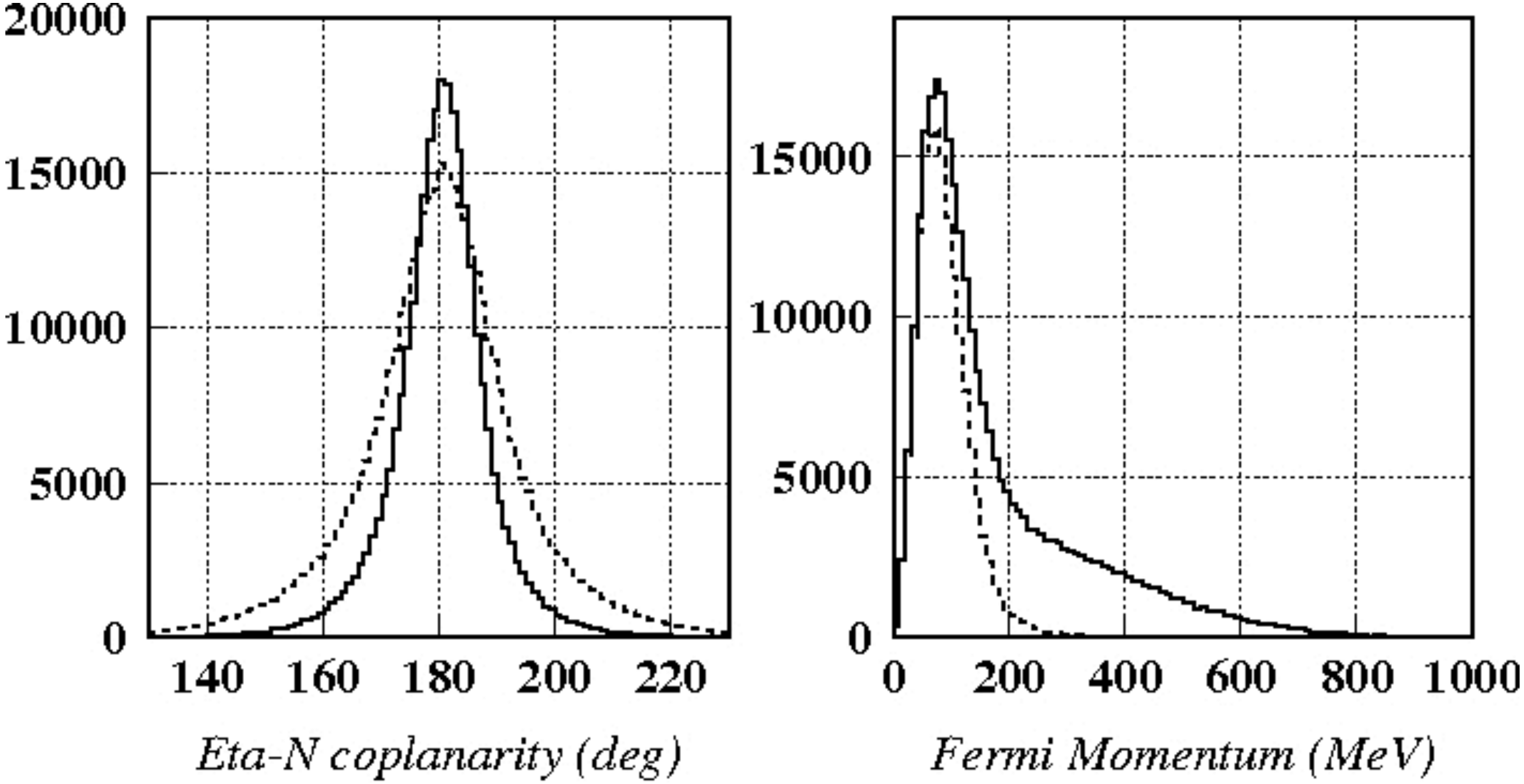

FIG. 5: Left: Coplanarity between the η and the free proton (solid line) and the quasi-free proton (dotted line): the smearing between the two distributions is due to the Fermi motion; Right: The Fermi momentum distribution before (solid line) and after (dashed line) the application of the bidimensional cuts (see text for details).

$\gamma + n + (p) \rightarrow \eta + n + (p)$ IM

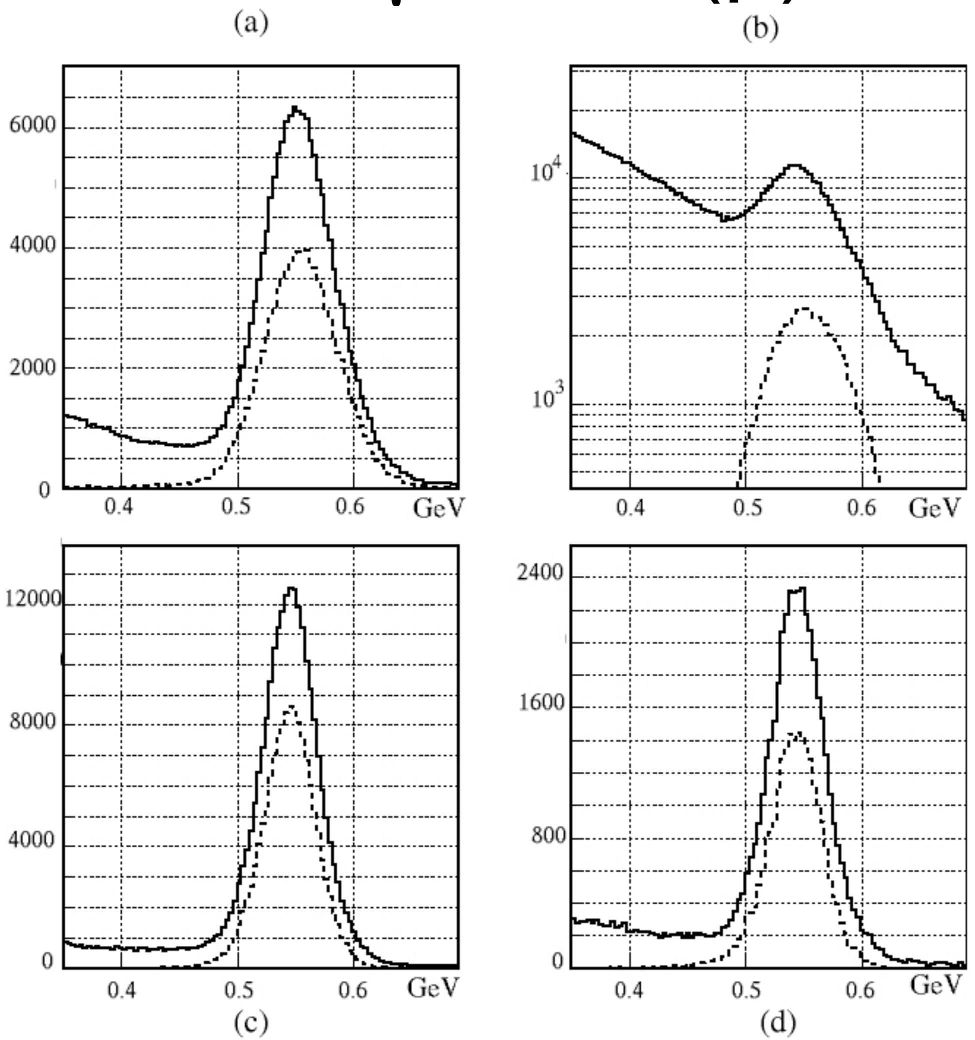

FIG. 3: The η invariant mass without cuts (solid line) and with the kinematical cuts (dotted line) for a central proton (a) and neutron (b) (in logarithmic scale), for a forward proton (c) and neutron (d).

$\gamma + n + (p) \rightarrow \eta + n + (p)$ $\cos(2\phi)$

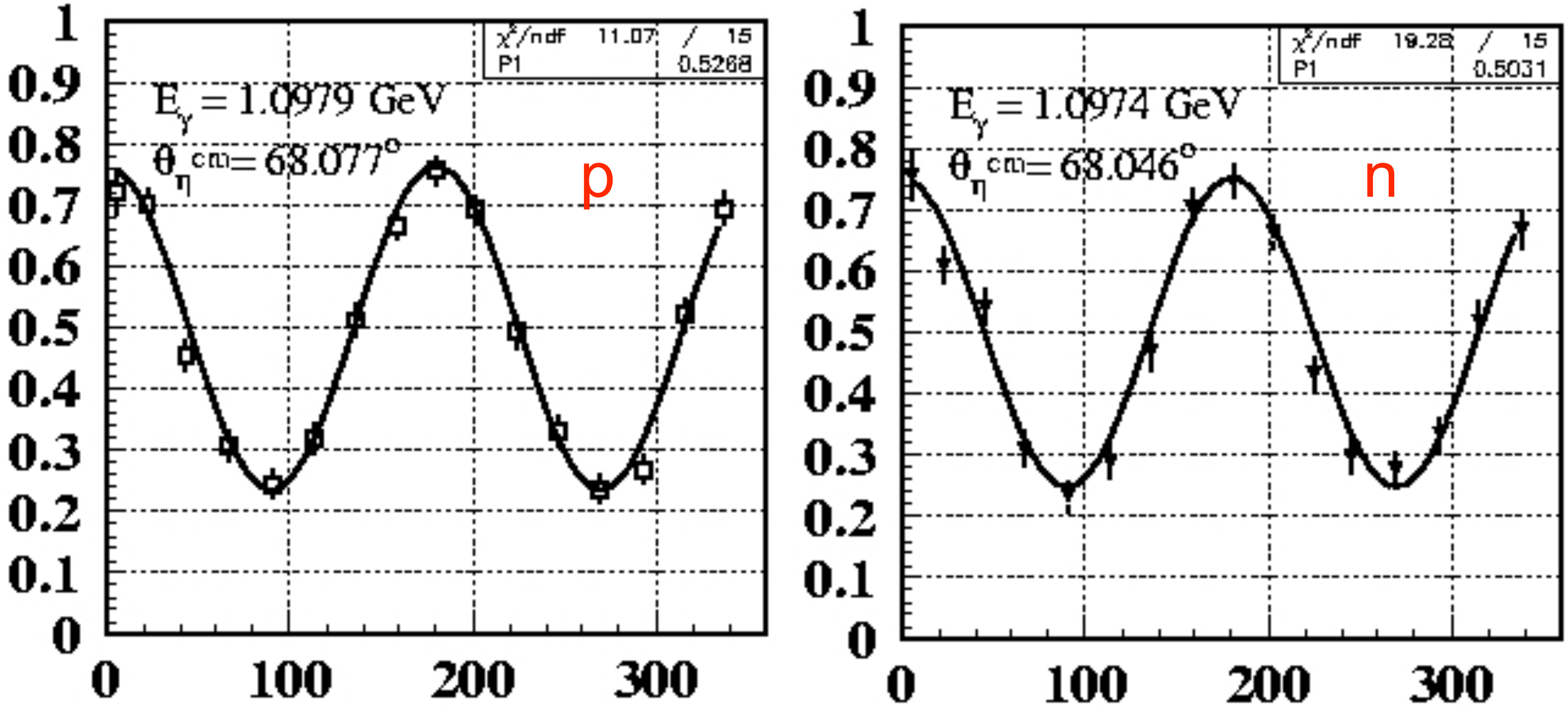

FIG. 4: The azimuthal distribution of the ratio (2) for the q.f. proton (a) and q.f. neutron (b) data in a fixed bin of E_γ and θ_η^{cm}.

$\gamma + n + (p) \rightarrow \eta + n + (p)$ $\Sigma(\theta)$ fp/qfp

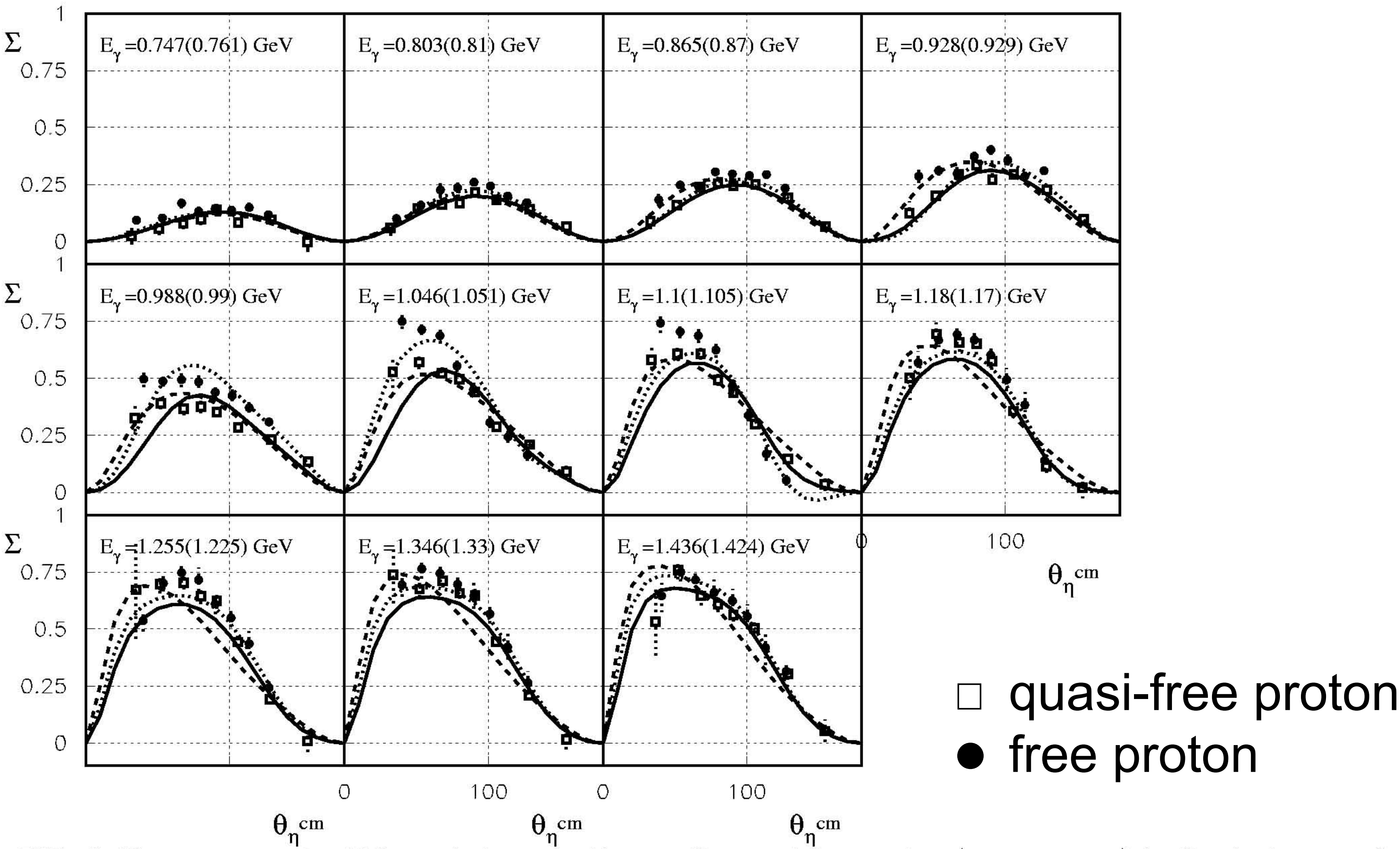

FIG. 6: Beam asymmetry Σ in η photoproduction on the quasi-free proton (open squares) in the deuteron and on the free proton (full circles)[2]. The energy value outside and inside parenthesis indicate the mean value of the bin for quasi free and free protons respectively. In dotted lines are illustrated the predictions of Maid2001 [7] for the free proton, in solid and dashed lines those for the quasi-free proton of Maid2001 [7] and the reggeized model [3], respectively (see text for details).

$\gamma + n + (p) \rightarrow \eta + n + (p)$ Tiator

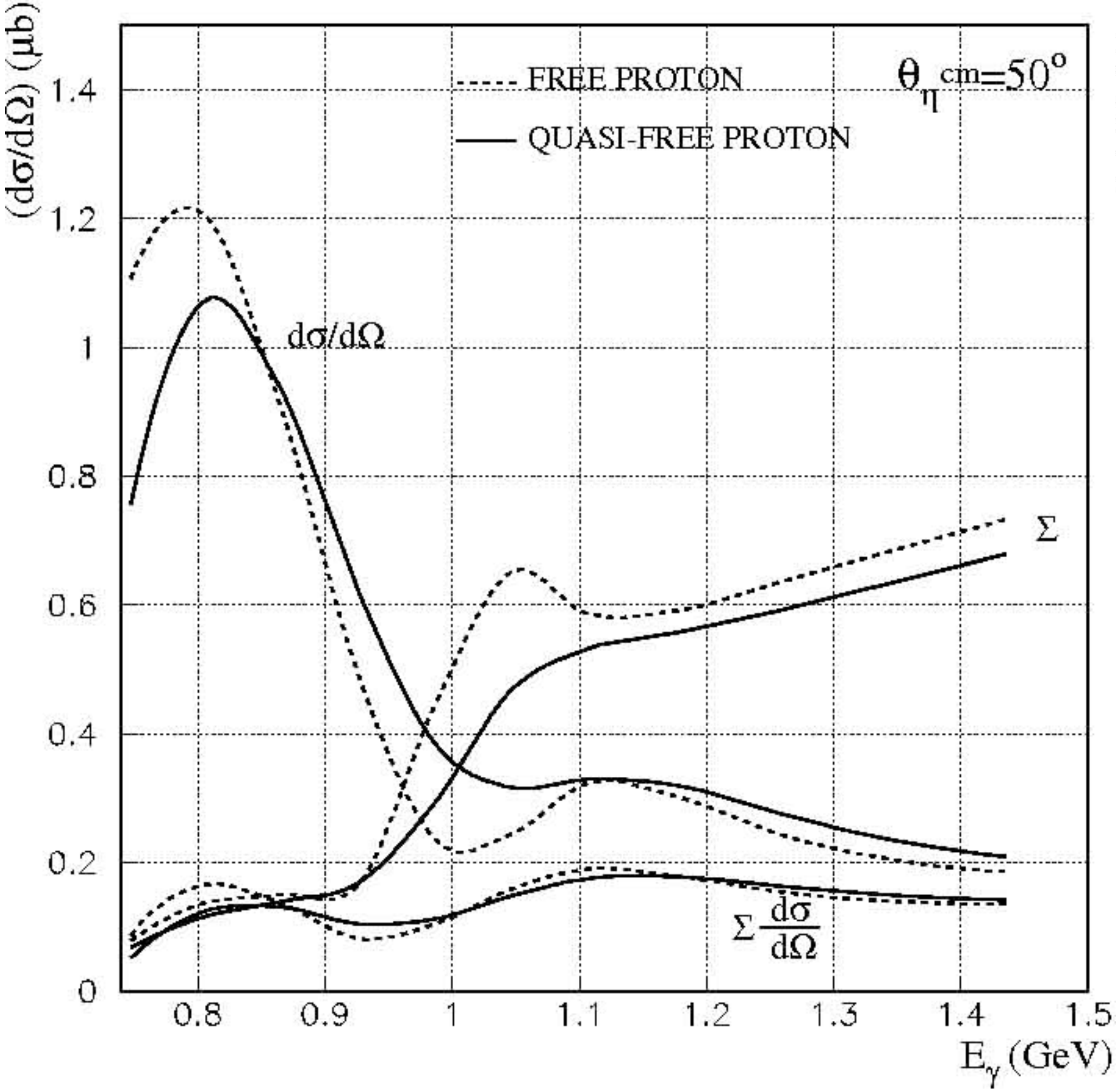

FIG. 7: Energy dependence of the differential cross section for $\gamma p \rightarrow \eta p$ calculated at $\theta = 50°$. The unpolarized cross section (5), the polarized cross section (6) and the beam asymmetry Σ are presented in the three pairs of curves for the free proton (dashed curves) and the quasi free proton (solid curves) respectively.

$\gamma + n + (p) \rightarrow \eta + n + (p)$ $\Sigma(\theta)$ qfn

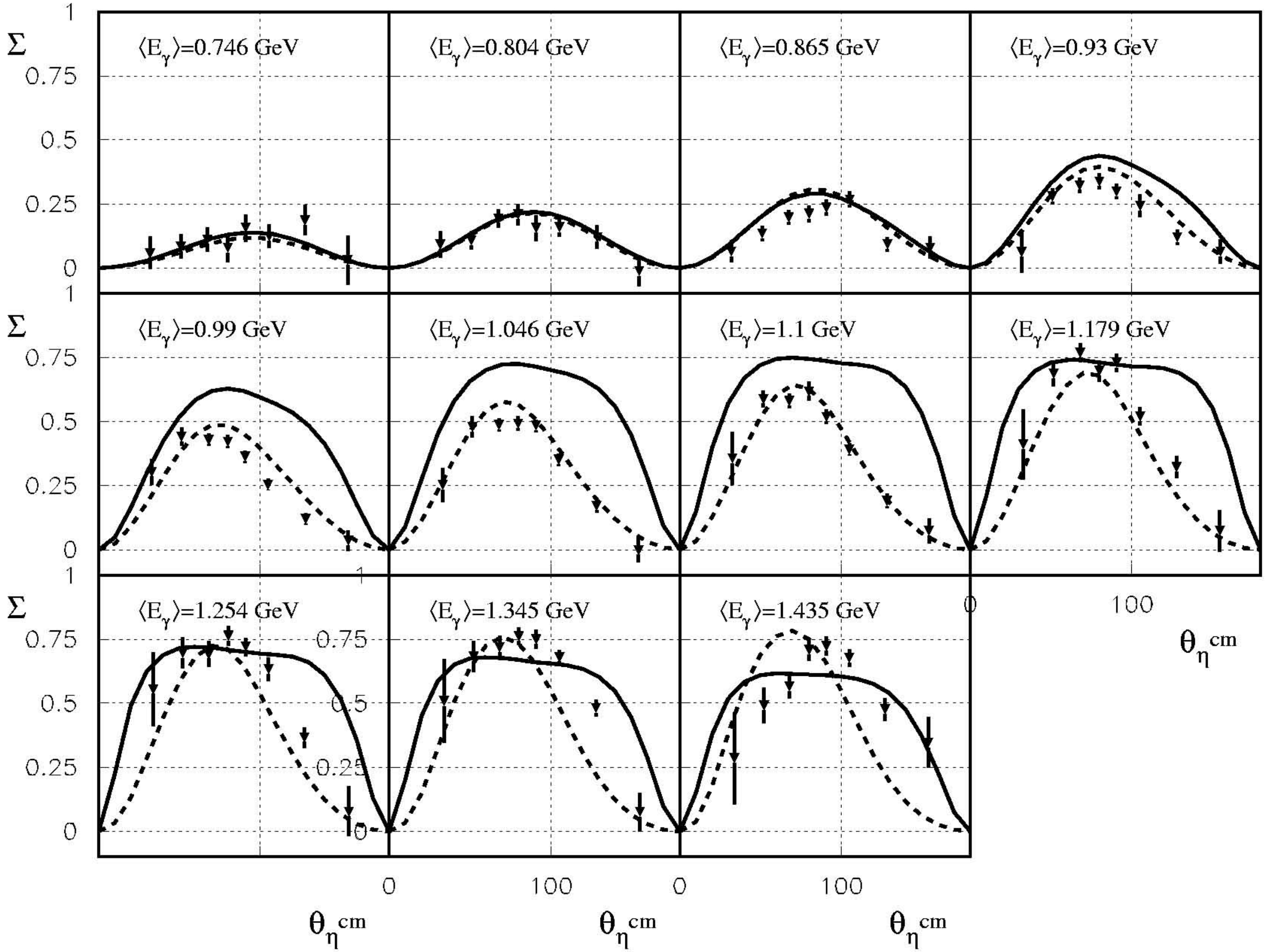

FIG. 8: Beam asymmetry Σ in η photoproduction on the quasi-free neutron in eleven energy bins, plotted as a function of the θ_η^{cm}. In each plot, the mean γ energy of the bin is also indicated. In solid and dashed lines are illustrated the predictions for neutrons of Maid2001 and of the reggeized model respectively (see text for details).

$\gamma + n + (p) \rightarrow \eta + n + (p)$ $\Sigma(\theta)$ qfn/qfp

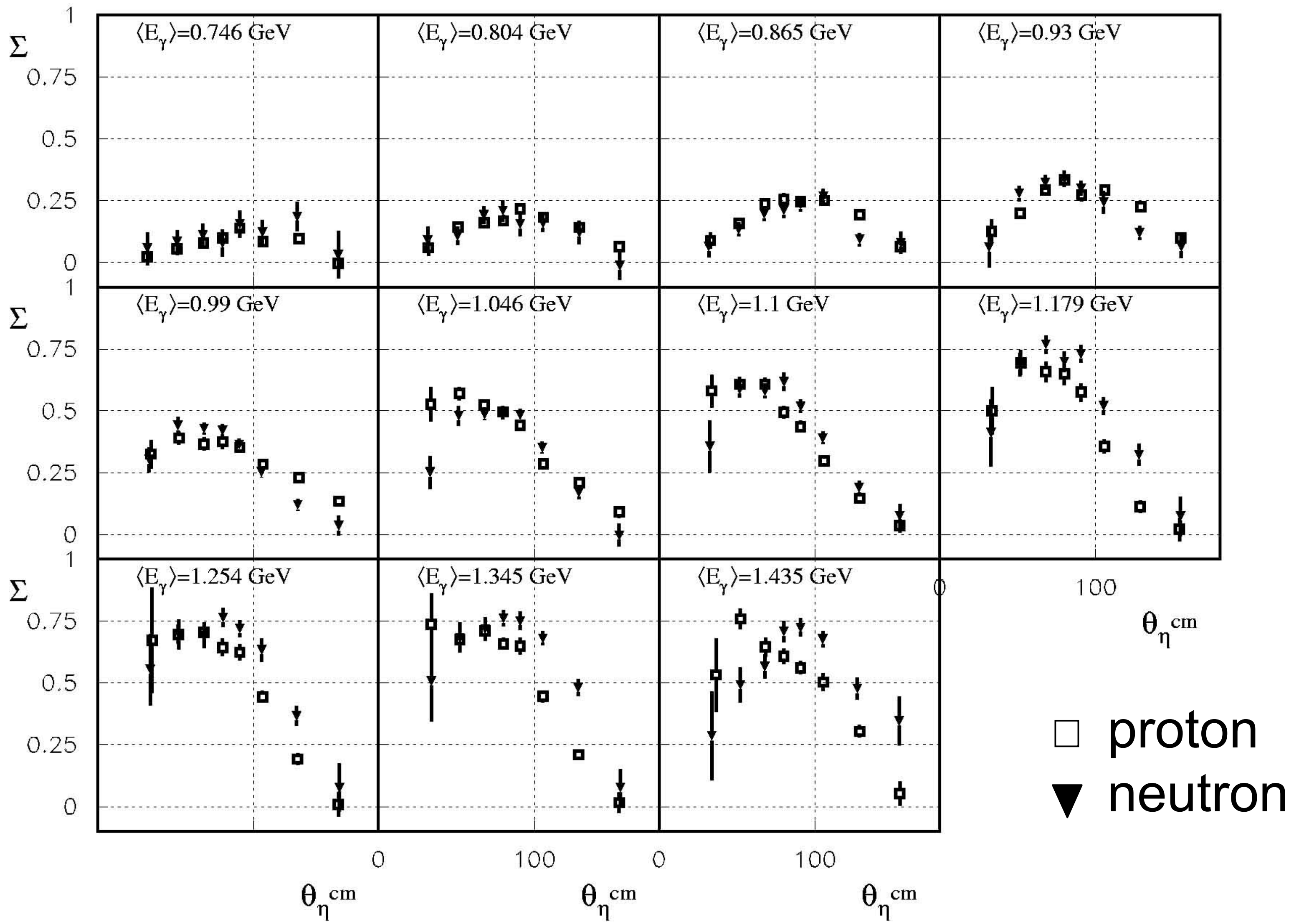

FIG. 9: Comparison between the beam asymmetry Σ in η photoproduction on the quasi-free proton (open squares) and the quasi-free neutron (full triangles) in the eleven energy bins, plotted as a function of the θ_η^{cm}. See text for details.

$\gamma + n + (p) \rightarrow \eta + n + (p)$ $\Sigma(E_\gamma)$ qfn/qfp

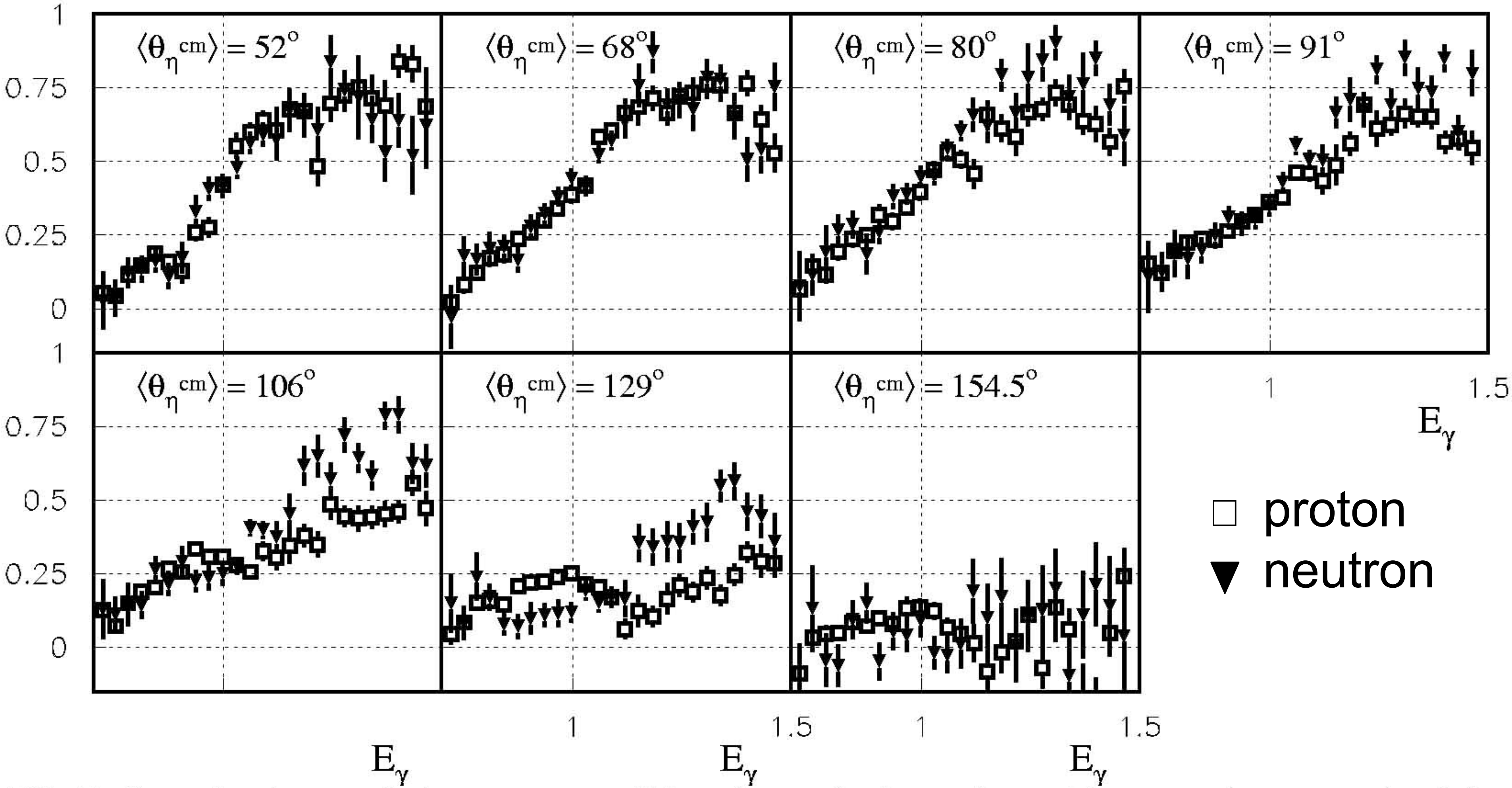

FIG. 10: Comparison between the beam asymmetry Σ in η photoproduction on the quasi-free proton (open squares) and the quasi-free neutron (full triangles) in seven angular bins, plotted as a function of the γ energy (intervals of $\simeq$25 MeV width.

$\gamma + n + (p) \rightarrow \eta + n + (p)$ Yield(Eγ)

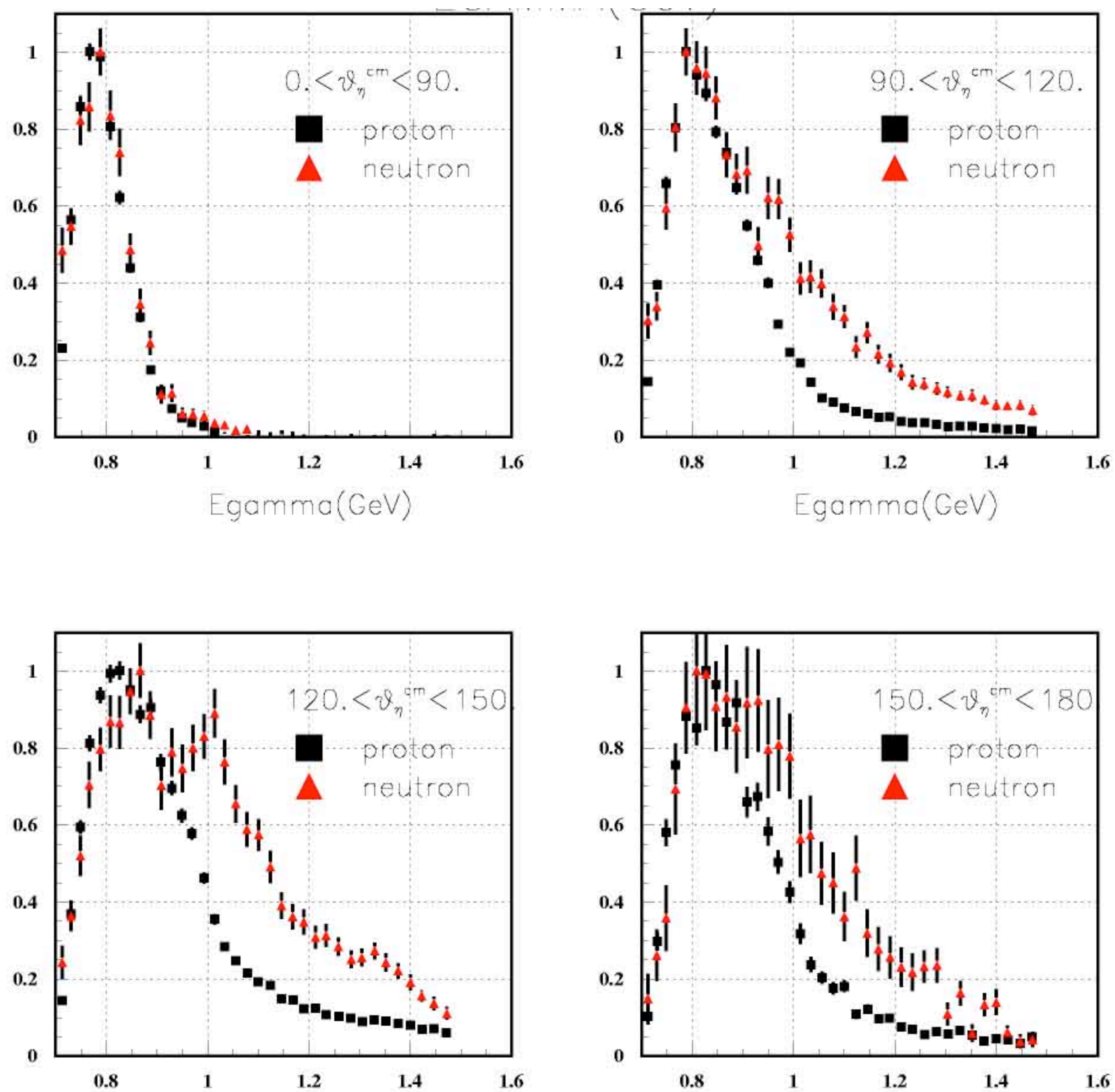

$\gamma + n + (p) \rightarrow \eta + n + (p)$ Yield(W)

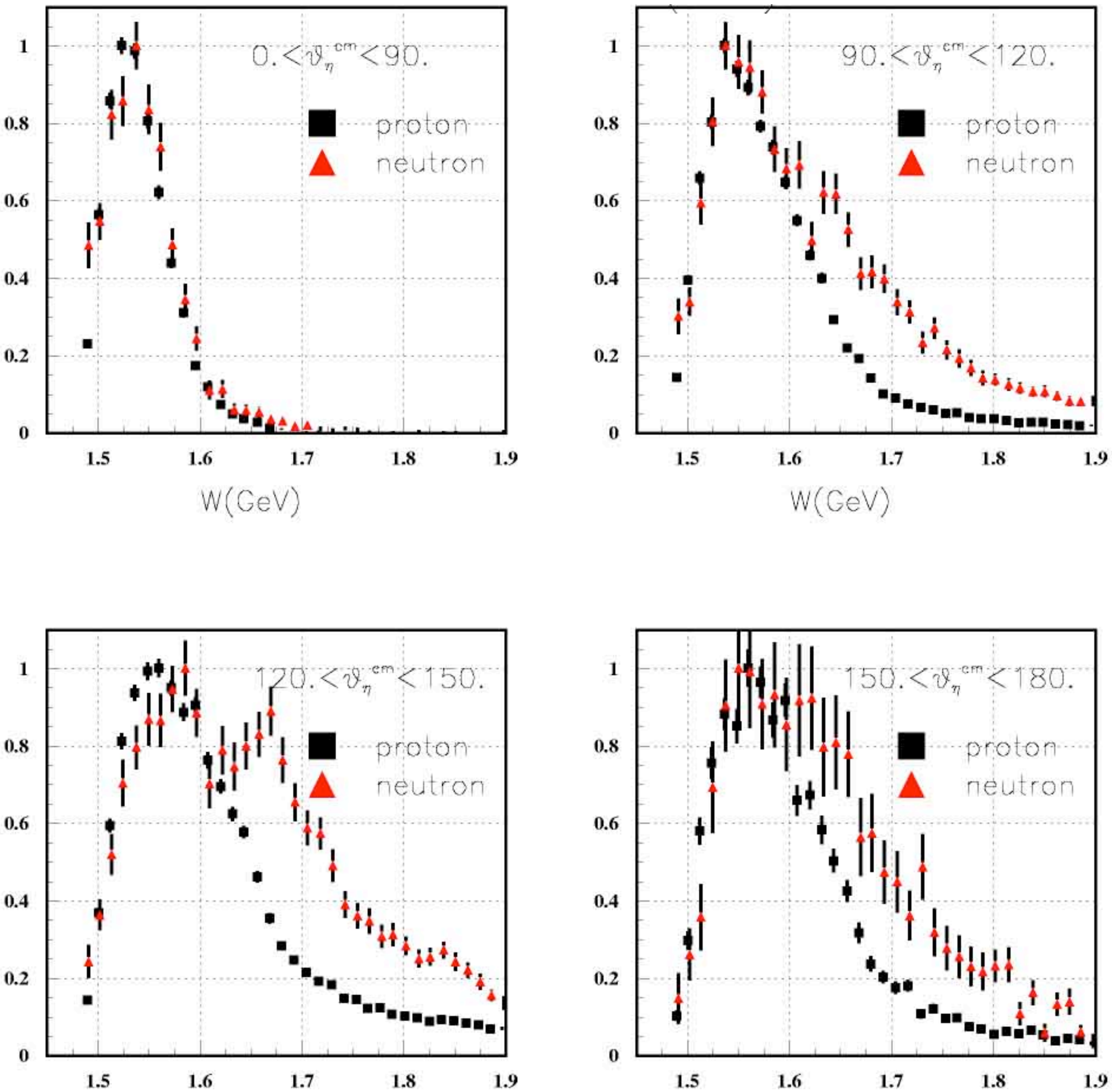

$\gamma + p \rightarrow \pi^0 + \eta + p \quad \sigma_{tot}$

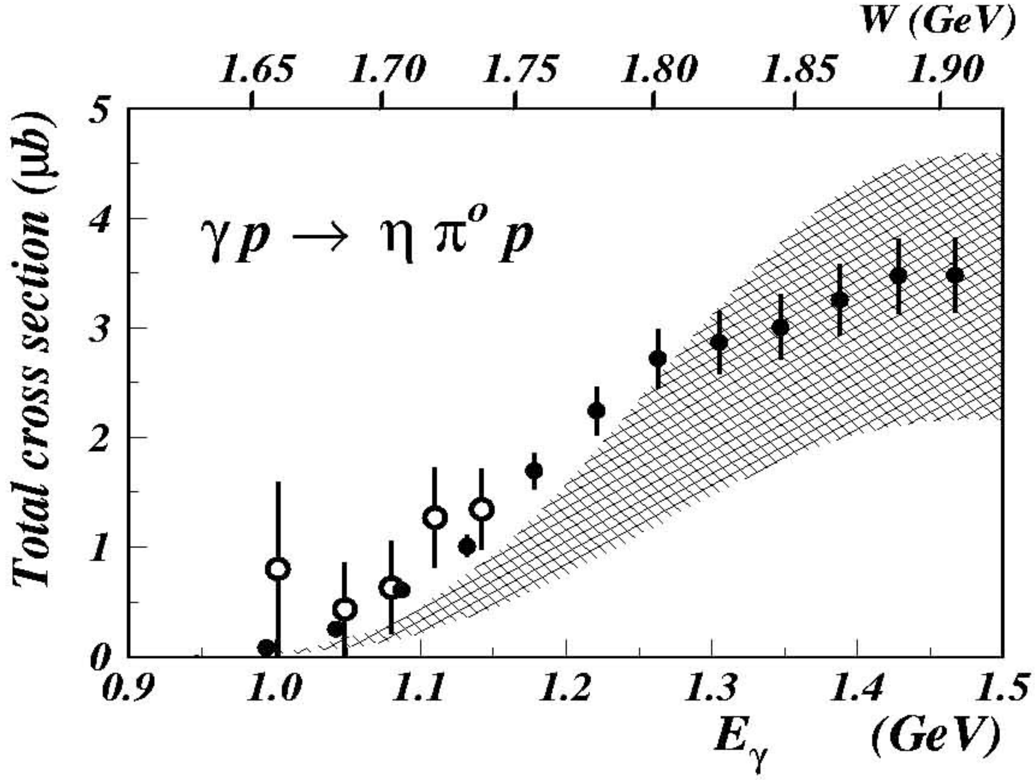

FIG. 2: Total cross section of the reaction $\gamma p \rightarrow \eta\pi^0 p$. The dots are the experimental data of this work. The open circles are from reference [9]. The results of the model of Ref. [6, 7] are given with their uncertainty by a hatched band of the figure. The uncertainty originates from the one on the $\gamma p\Delta(1700)$ coupling which was taken from the PDG [10]

$\gamma + p \rightarrow \pi^0 + \eta + p$ IM

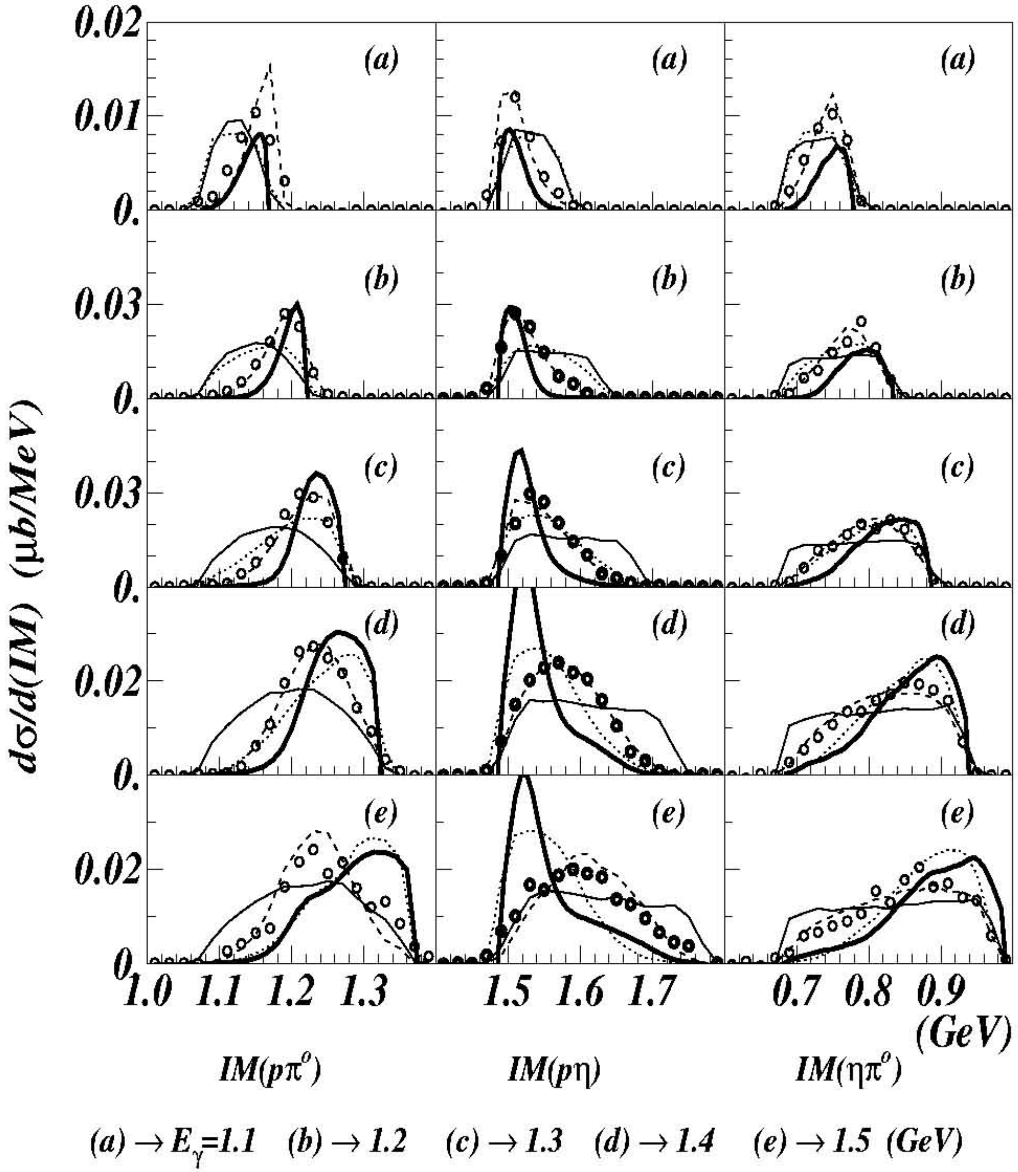

FIG. 3: For the reaction $\gamma p \rightarrow \eta\pi^0 p$, spectra of invariant mass of $(p\pi^0)$, $(p\eta)$ and $(\eta\pi^0)$ groups of the final state, presented in 3 different columns. The various rows, labeled (a),...,(e) correspond to beam energies given at the bottom of the figure. In empty circles are the experimental results, in thin line for $\gamma p \rightarrow \eta\pi^0 p$ with a 3-body phase space in the final state, in dashed line for $\gamma p \rightarrow \eta\Delta$ with $\Delta \rightarrow \pi^0 p$, in dotted lines for $\gamma p \rightarrow \pi^0 S_{11}$ with $S_{11} \rightarrow \eta p$. The theoretical curves, given by thick lines, are the central values of the results of the model of Ref. [6, 7] .

It looks like:

$\gamma + p \rightarrow \eta + \Delta$

$\Delta \rightarrow \pi^\circ + p$

$\gamma + p \rightarrow \pi^0 + \eta + p \quad \Sigma$

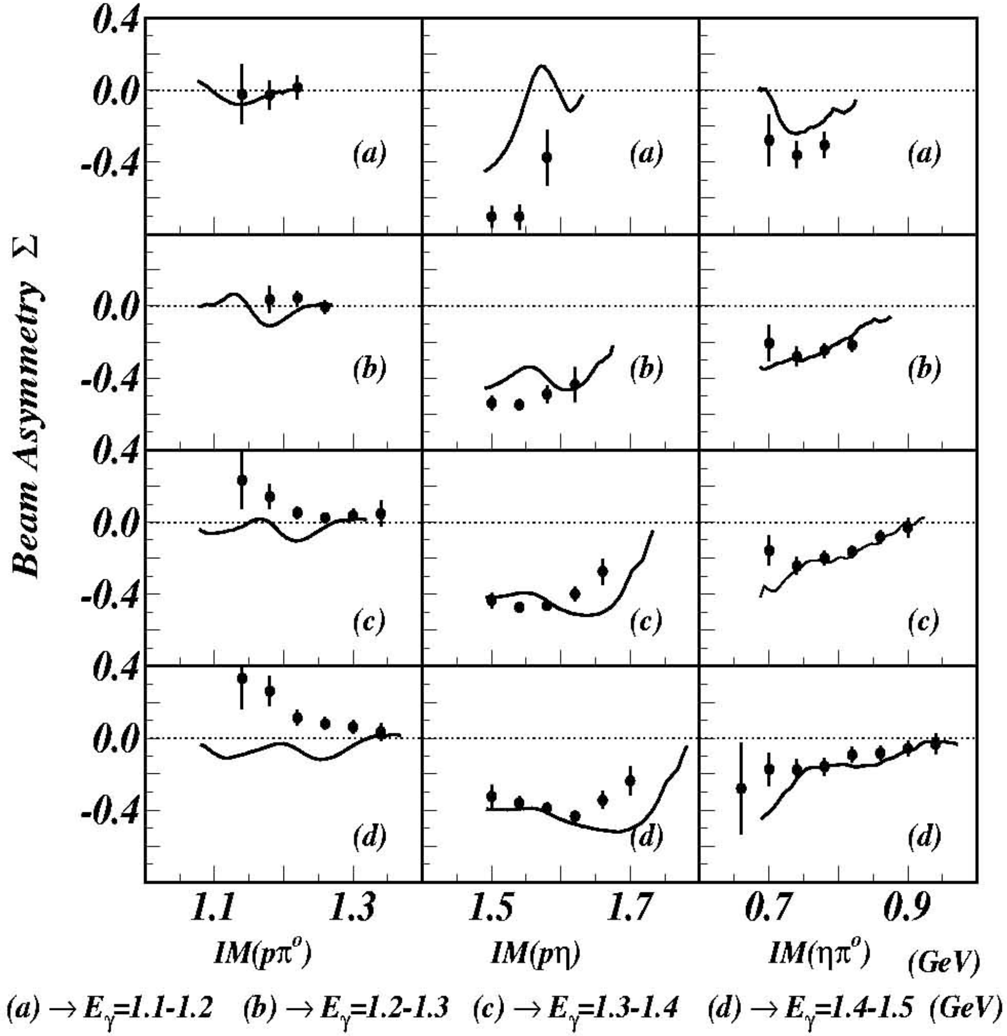

FIG. 4: Beam asymmetry of the reaction $\gamma p \rightarrow \eta \pi^0 p$. The theoretical results are calculated with the model of Ref. [6, 7]

Compton Scattering Kinematics

2. The maximum energy lost by the electrons after an elastic scattering with a laser photon is given by the maximum energy acquired by the photon:

$$E_{el}^{0} - E_{el}^{scatt} = E_{\gamma\,\max} = \frac{4\gamma^2 E_{laser}}{1 + \frac{4\gamma E_{laser}}{m_e}} \approx 4\gamma^2 E_{laser}$$

This energy loss is measured by the displacement **d** of the scattered electrons from the primary electron beam after the first magnetic dipole. For the ESRF electron energy of 6.03 GeV and a UV laser line of 3.53 eV, the energy loss is 1.487 GeV and corresponds to an electron displacement at the position of the Graal tagging detector: $\boldsymbol{d}$ **≈ 52.3 mm**.

The microstrips of the Graal tagging detector measure the displacement $\boldsymbol{d}$ of the scattered electrons from the main orbit and therefore the energy lost by the electrons (and acquired by the gamma-rays):

$$E_\gamma \propto d$$

Compton Scattering Kinematics

3. From the relativistic kinematics of Compton scattering:

$$E_{\gamma\,\max} = \frac{4\gamma^2 E_{laser}}{1 + \frac{4\,\gamma\,E_{laser}}{m_e}} \approx 4\gamma^2 E_{laser} \quad \text{and} \quad \frac{d\,E_\gamma}{E_\gamma} \approx 2\frac{d\gamma}{\gamma} \quad \text{or} \quad \frac{d\gamma}{\gamma} \approx \frac{1}{2}\frac{d\,E_\gamma}{E_\gamma}$$

and in general from relativistic kinematics:

$$\beta\,d\beta = \left(\frac{1}{\gamma^2}\right)\frac{d\gamma}{\gamma} \approx \frac{1}{2}\left(\frac{1}{\gamma^2}\right)\frac{d\,E_\gamma}{E_\gamma} \quad \text{or} \quad \Delta\beta \approx \frac{1}{2}\left(\frac{1}{\gamma^2}\right)\frac{\Delta E_\gamma}{E_\gamma}$$

since at the ESRF:

$$\gamma = \frac{E_e}{m_e} = \frac{6030}{0.511} = 11\,800; \qquad 2\,\gamma^2 \approx 2.8\cdot 10^8$$

we have:

$$\Delta\beta \approx \frac{1}{2}\left(\frac{1}{\gamma^2}\right)\frac{\Delta E_\gamma}{E_\gamma} \approx \frac{1}{2{,}8\cdot 10^8}\cdot\frac{\Delta E_\gamma}{E_\gamma} \approx 0.4\cdot 10^{-8}\,\frac{\Delta E_\gamma}{E_\gamma} \approx 0.4\cdot 10^{-8}\,\frac{\Delta d}{d}$$

The error in β is reduced by eight orders of magnitude with respect to the relative error in ***d*** (the displacement of the scattered electrons from the main orbit).

Graal Tagging Microstrips

Schematic description of the tagging detector in more details.
Vertical cut: the electrons fly out of the screen.

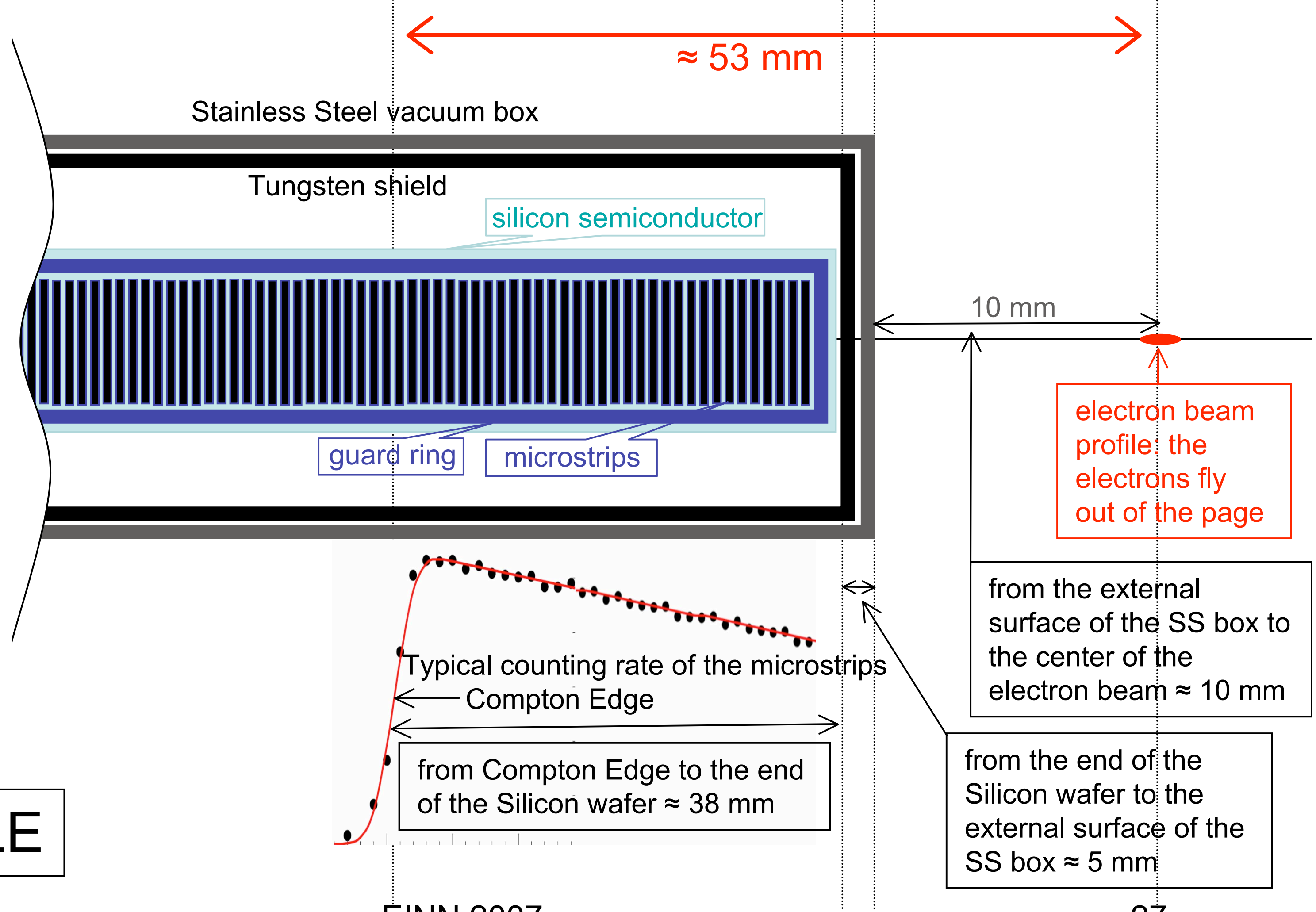

NOT IN SCALE

Distribution of Graal Data

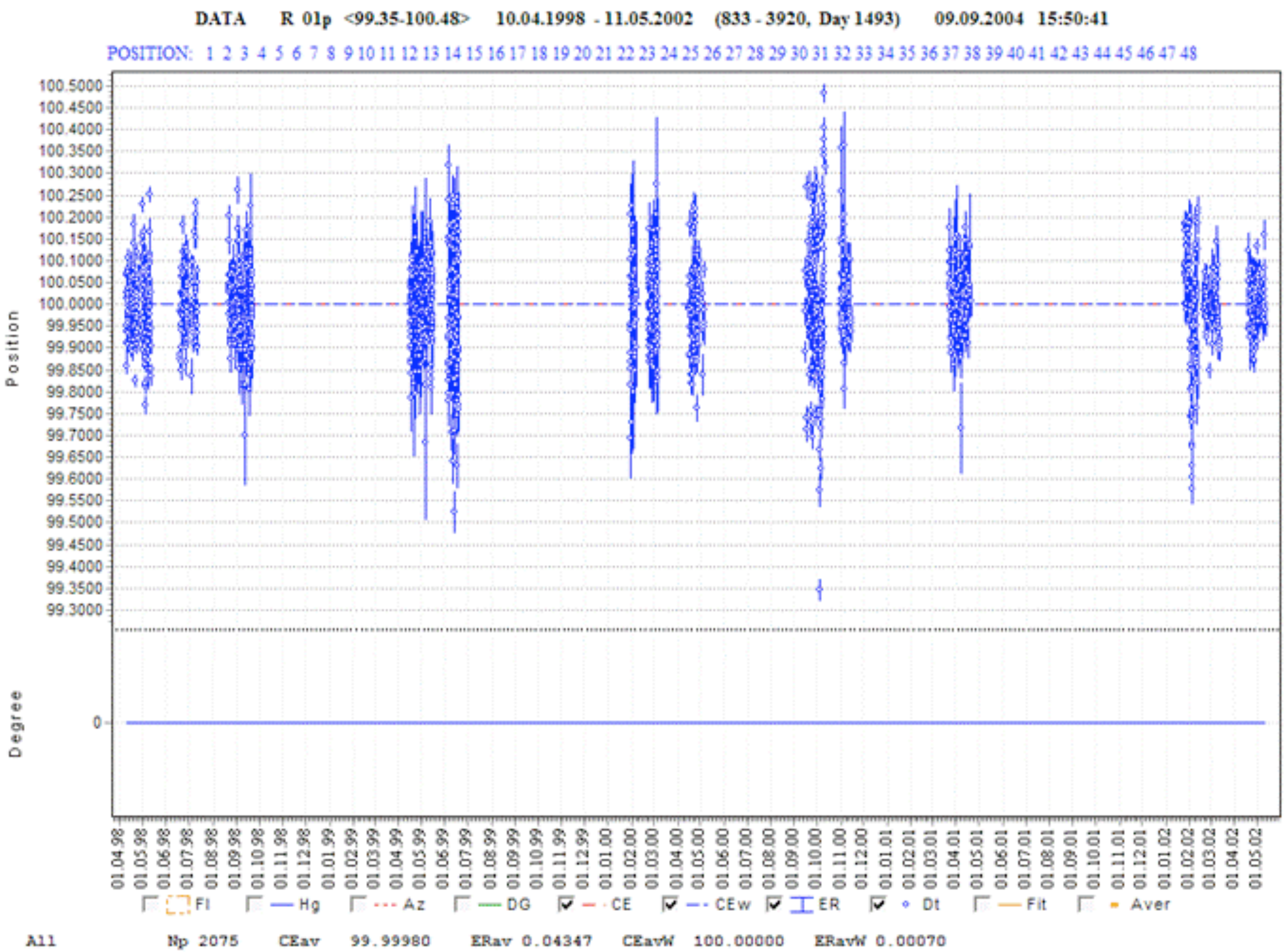

Daily Compton Edges Distributions

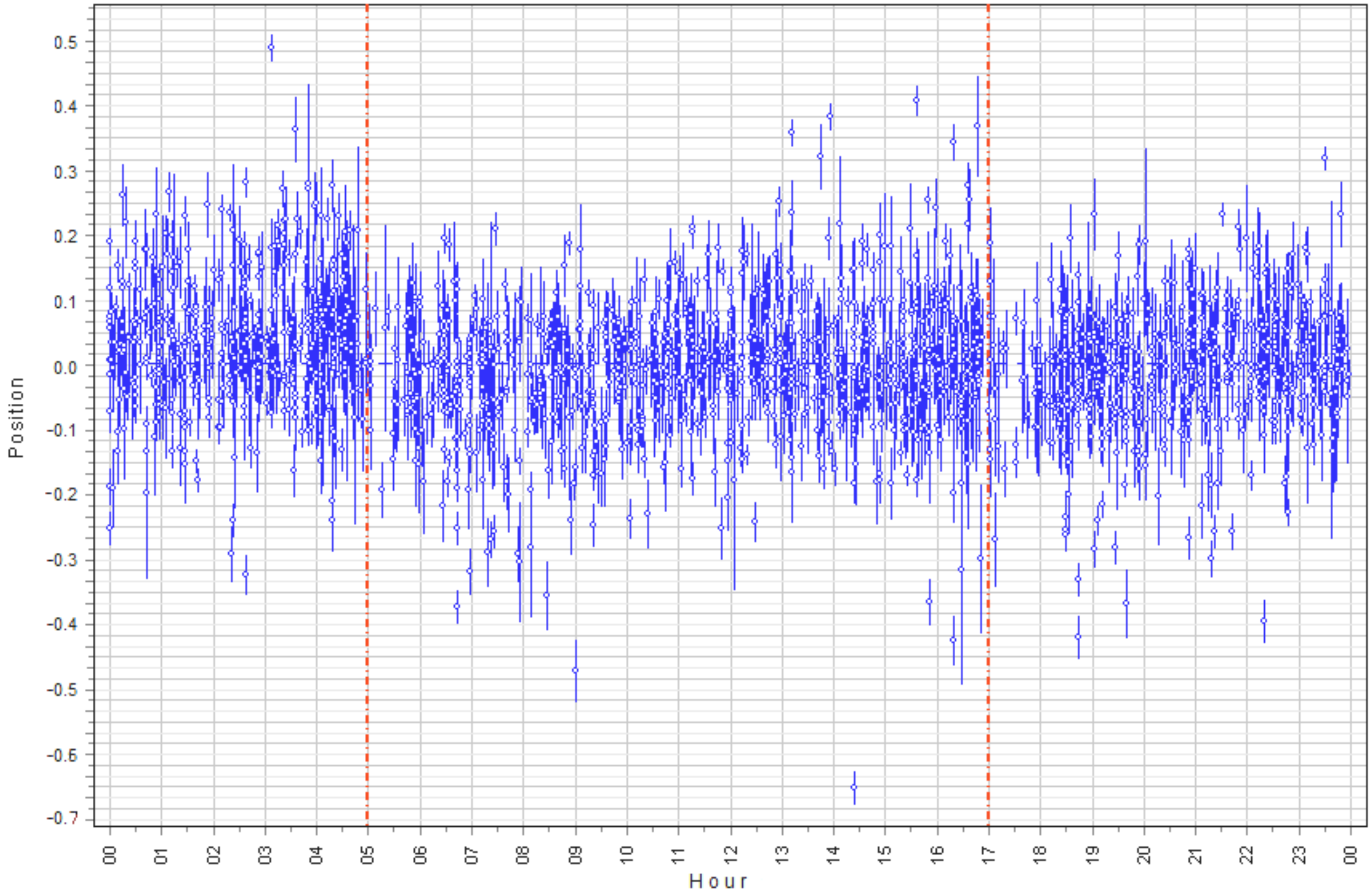

Experimental data plotted as a function of (solar) hour, showing their daily variation. The dispersion of data around the average, taken arbitrarily at zero, is expressed in fractions of microstrip (300 micrometers width or about 7 MeV for one microstrip).

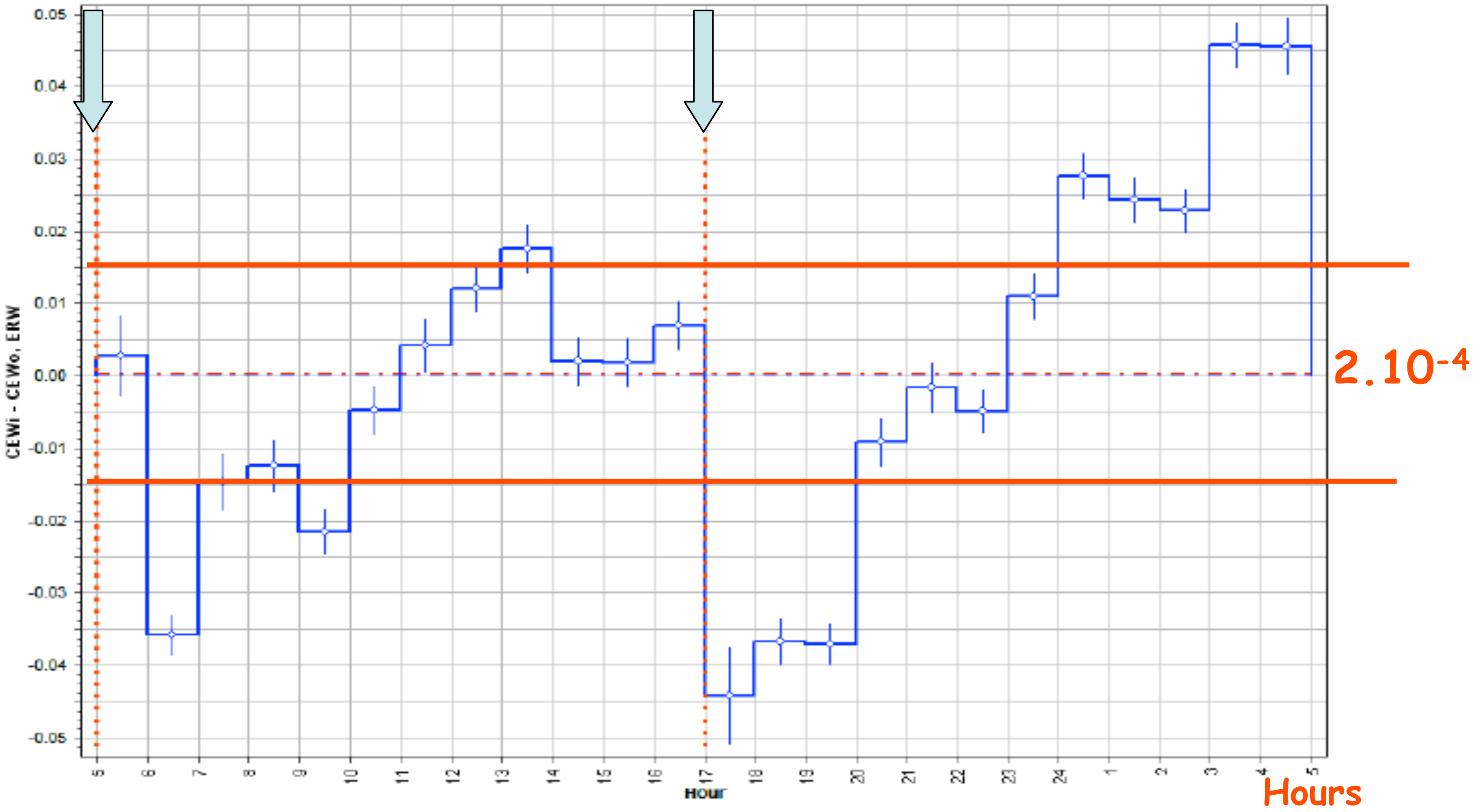

Same as the previous figure, but each point is the average over one hour. The dotted lines show the refill time of the machine corresponding to a possible change in the temperature of the tagging detector or the position of the beam. The average is expressed in microstrip fractions (0.01 = 3μm).

Graal Beam Orientation on the Earth

The Graal beam points approximately to the S-W

≈S-W (225°)

230.6°

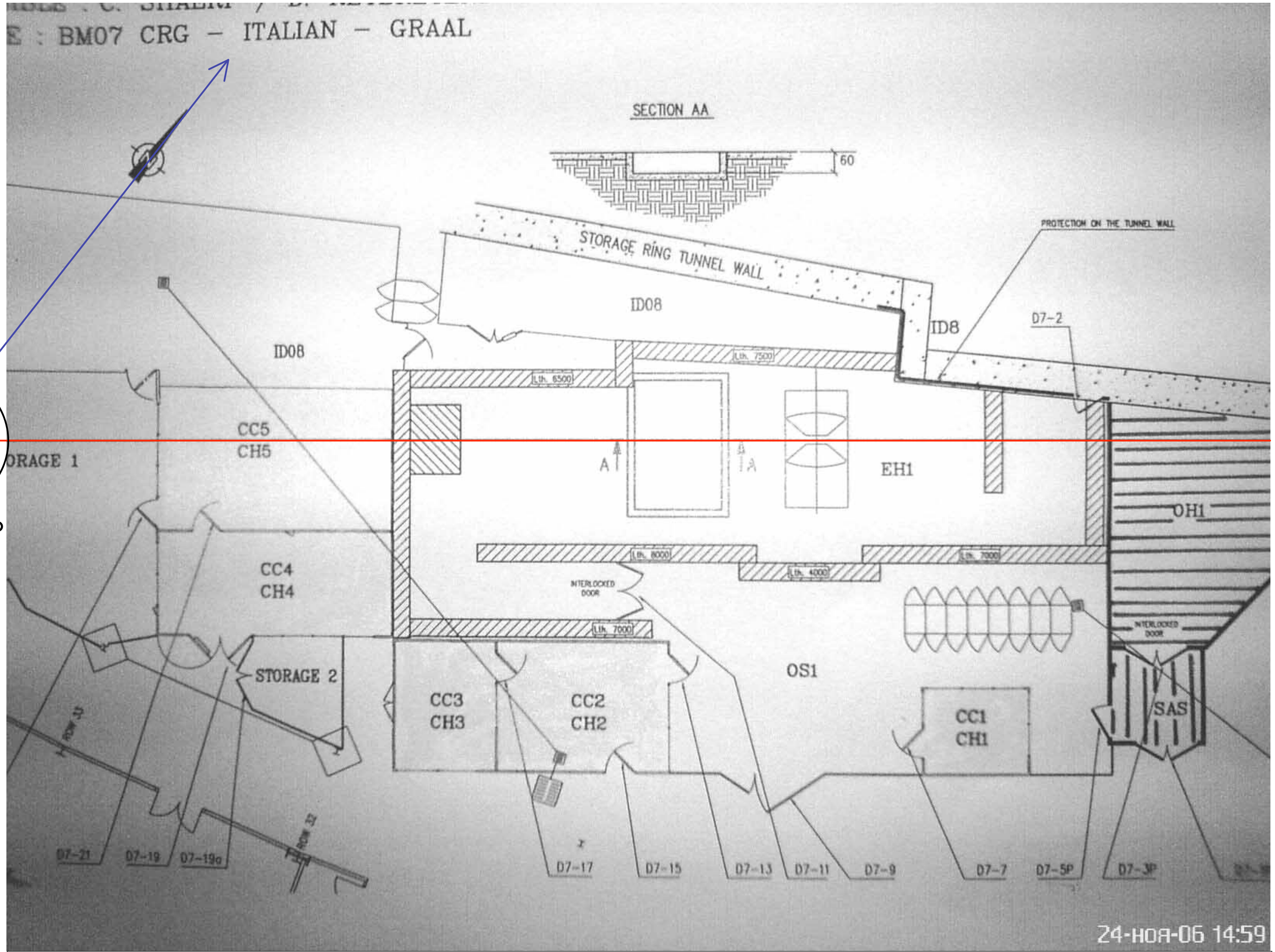

Earth rotation around its axis: $\omega = 7.3 \cdot 10^{-5}$ rad s^{-1}

Earth rotation around the sun: $\omega = 2 \cdot 10^{-7}$ rad s^{-1}

Graal Rotations and the CMB

North

Earth rotation around its axis:
$\omega = 7.3 \cdot 10^{-5}$ rad s^{-1}
Earth rotation around the sun:
$\omega = 2 \cdot 10^{-7}$ rad s^{-1}

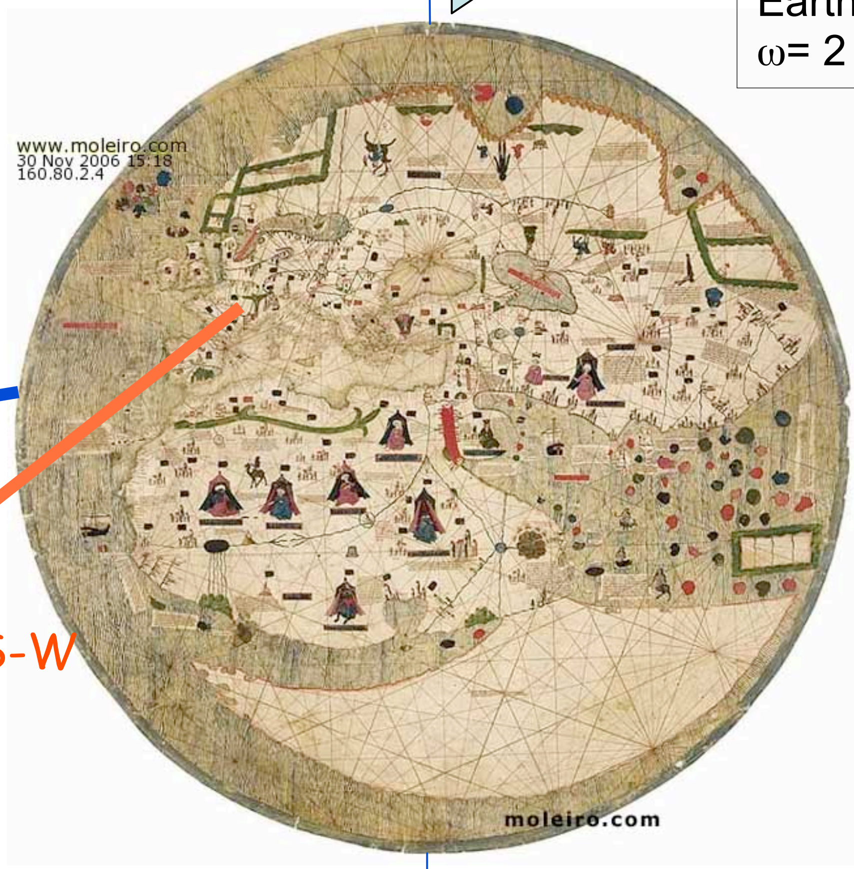

CMB (97° / NS Axis)

GRAAL beam line
approximately to the S-W

mappamondo estense 1450

Compton Edge Positions vs CMB Dipole

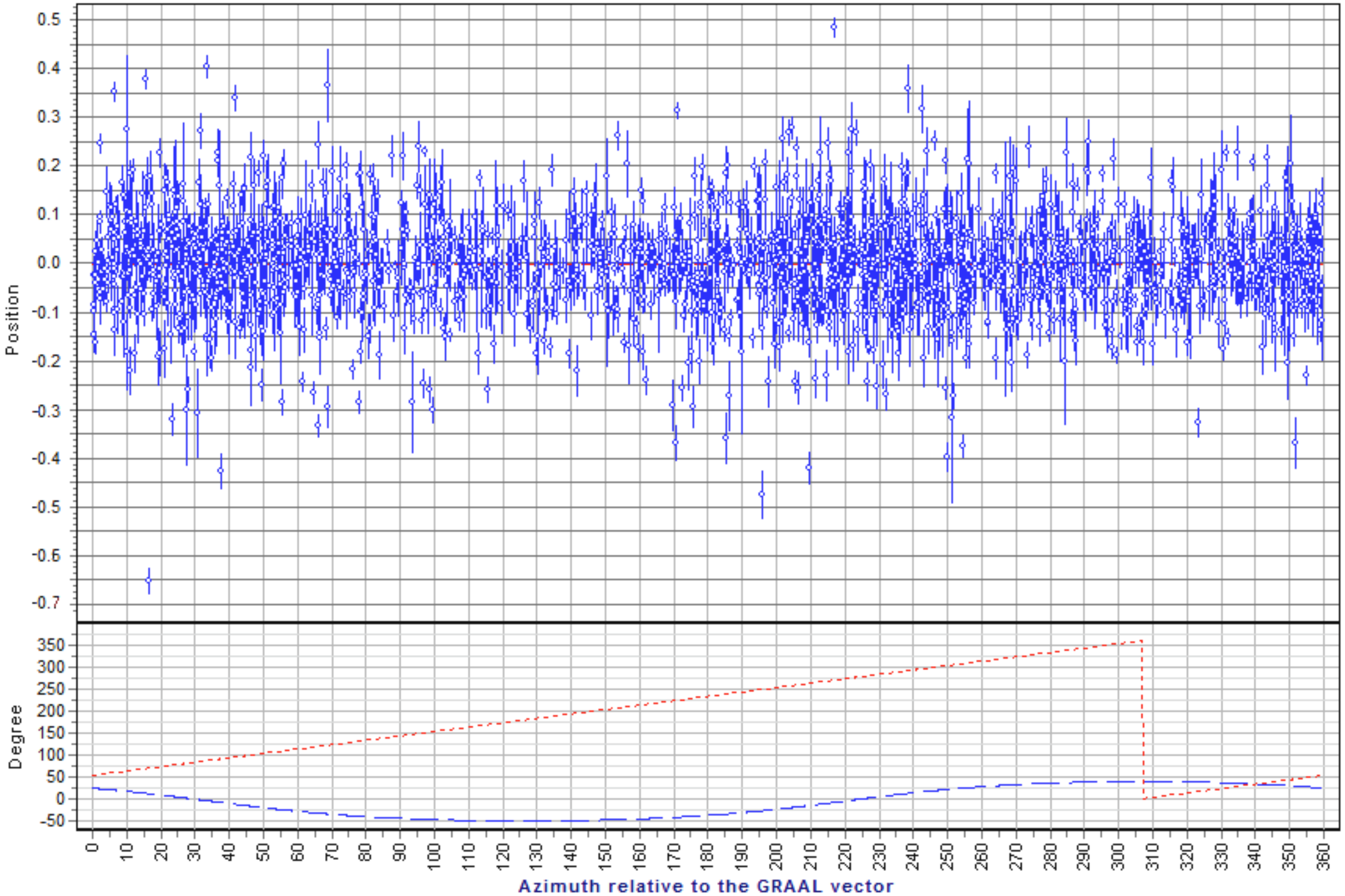

Experimental data plotted as a function of the azimuth (above); below, the variation of the angle between the beam and the CMB dipole decomposed to azimuth (dotted) and declination (dashed) angles is shown.

Preliminary Result

Assuming an error of

$$2 \cdot 10^{-4}$$

in our determination of the position of the Compton Edge, we could arrive to an estimated upper limit on the asymmetry of the velocity of light of:

$$\Delta\beta \approx \frac{1}{2}\left(\frac{1}{\gamma^2}\right)\frac{\Delta E_\gamma}{E_\gamma} \approx 0.4 \cdot 10^{-8}\,\frac{\Delta d}{d} \approx 0.4 \cdot 10^{-8} \cdot 2 \cdot 10^{-4} \approx 10^{-12}$$

Considering that we have analyzed old data and we have not been able to reconstruct completely the status of the system - accelerator + tagging detector - during our runs we have published the more conservative number:

$$3 \cdot 10^{-12}$$

An Optimistic View of the Future

In conclusion if optimistically we assume a systematic error of 2.5 μm in the distance between the position of the Compton Edge and the electron beam, we have:

$$\frac{(\Delta d)_{sys}}{d} \approx \frac{2.5\,\mu m}{52.3\,mm} \approx \quad 5\cdot 10^{-5} \quad \approx \quad \frac{(\Delta E_\gamma)_{stat}}{E_\gamma}$$

and we can hope to be able to verify the isotropy of the velocity of light with respect to some absolute reference frame with a precision of:

$$\Delta\beta \approx \frac{1}{2}\left(\frac{1}{\gamma^2}\right)\frac{\Delta E_\gamma}{E_\gamma} \approx 0.4\cdot 10^{-8}\,\frac{\Delta E_\gamma}{E_\gamma} \approx 0.4\cdot 10^{-8}\cdot 5\cdot 10^{-5} \approx 2\cdot 10^{-13}$$